Electromagnetic characterization of conductor-backed media using stepped rectangular waveguide

THESIS

Avian Y. Hughes, Capt, USAF

AFIT-ENG-MS-19-M-033

DEPARTMENT OF THE AIR FORCE
AIR UNIVERSITY

AIR FORCE INSTITUTE OF TECHNOLOGY

Wright-Patterson Air Force Base, Ohio

AFIT-ENG-MS-19-M-033

ELECTROMAGNETIC CHARACTERIZATION OF CONDUCTOR-BACKED MEDIA USING STEPPED RECTANGULAR WAVEGUIDE

THESIS

Presented to the Faculty

Department of Engineering Electrical Engineering

Graduate School of Engineering and Management

Air Force Institute of Technology

Air University

Air Education and Training Command

in Partial Fulfillment of the Requirements for the

Degree of Master of Science in Electrical Engineer

Avian Y. Hughes, B.S.E.E.

Capt, USAF

March 21, 2019

AFIT-ENG-MS-19-M-033

ELECTROMAGNETIC CHARACTERIZATION OF CONDUCTOR-BACKED MEDIA USING STEPPED RECTANGULAR WAVEGUIDE

THESIS

Avian Y. Hughes, B.S.E.E.
Capt, USAF

Committee Membership:

Dr. M. J. Havrilla
Chair

Dr. P. J. Collins, PhD
Member

Dr. J. A. Jackson, PhD
Member

Acknowledgements

Anything begun in vanity ends in humility.

Many thanks to everyone that put their effort into helping me graduate.

Avian Y. Hughes

Abstract

A new single stepped-iris waveguide technique is used to nondestructively determine the permittivity and permeability of conductor-backed media. This thesis will demonstrate a proof-of-concept that obtains two independent reflection measurements with a magnetic radar absorbing material (magRAM). Using a two measurement procedure, in which, the first measurement will apply a single rectangular waveguide to a known conductor-backed absorbing material under test (MUT) and the second measurement will insert a stepped-iris in between the single rectangular waveguide and MUT reducing the aperture to retrieve two independent electromagnetic properties (i.e. permittivity and permeability). The theoretical reflection coefficients are obtained using a rigorous full-wave solution combined with a mode matching method at the waveguide and iris regions. Additionally, a root search algorithm is used to extract electromagnetic properties of magRAM by comparing the theoretical and experimentally measured reflection coefficients. The experimental measurements of a commercial magRAM using a network analyzer will demonstrate the feasibility of the stepped-iris approach. Plots of the extracted permittivity and permeability of the MUT are analyzed to validate the stepped-iris material characterization technique.

Table of Contents

Page

List of Figures

ELECTROMAGNETIC CHARACTERIZATION OF CONDUCTOR-BACKED MEDIA USING STEPPED RECTANGULAR WAVEGUIDE

I. Introduction

Electromagnetic material characterization with conductor-backed magnetic radar absorbing material (magram) by in situ measurements is challenging. In situ measurements identify the electromagnetic properties (i.e., permittivity and permeability), of the concerned or damaged material in its original place or position. Electromagnetic material characterization is the process to determine the electromagnetic properties of a material under applied electromagnetic field over a range of frequencies. Permittivity is the measure of how susceptible a dielectric polarizes (or aligns) in response to an electric field. Likewise, permeability is the measure of how susceptible a material magnetizes (or aligns) in response to a magnetic field.

1.1 Background

These measurements focus on evaluating materials nondestructively (without causing damage to the material). In contrast, cutting or tearing parts off the material of interest for measurements is classified as a destructive technique. Nondestructive measurements are taken noninvasively (not inserting or entering any device internally) such as penetrating or probing inside the material of interest for measurements. The above-mentioned measurements are invaluable because, in cases where damaged or corrupted material is observed, an estimate of the material's electromagnetic properties is useful and complements visible and mechanical inspections. Several destructive reflection/transmission techniques have been developed for characterizing the electro-

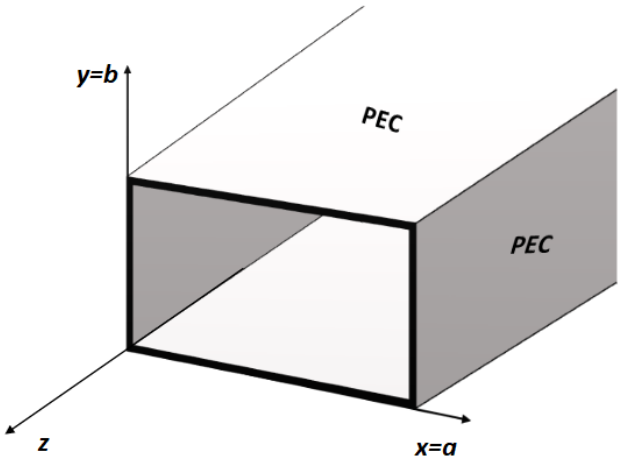

Figure 1. Open-ended Rectangular Waveguide. This hollow structure consists of four finite conducting walls with open-ends on both sides of the rectangle. A rectangular coordinate system is appended to the face of the open-ended rectangular waveguide cross section (bold) where the height corresponds to the y-axis, the length corresponds to the x-axis and the z-axis corresponds to the direction of wave propagation.

magnetic properties of materials under laboratory conditions, but the majority of the developments are of no avail because transmission measurements are typically not available and material destruction is not allowed in field use applications [1].

To overcome this shortfall, research has focused on directly applying the field to the material under test (MUT), and a favorable technique used is the open-ended rectangular-waveguide probe. An open-ended waveguide, shown in Fig. 1, is a two-port device that typically has a rectangular cross-section; the structure is open on one end and terminated on the other end by a conductor i.e., a perfect electric conductor (PEC) [2]. In Fig. 1 the PEC walls helps direct electromagnetic energy through the open end, where a, b, z correspond to x, y, z respectively. This energy is subsequently used to interrogate the electromagnetic properties of materials. These devices are normally enticing since they can be used to determine the electromagnetic properties of a material nondestructively and are commercially available.

Most nondestructive (NDE) and noninvasive experiments and research regarding open-ended rectangular-waveguide probes denote single waveguide probe geometries

that primarily focus on dielectric materials. A dielectric is an electrical insulator that can be polarized by an applied electric field, in which positive charges are displaced in the direction of the field and negative charges are moved in the opposite direction. Further, when dielectric materials are placed in an electric field, hardly no current flows in them. Recall, single waveguide probes are terminated by a conductor in the waveguide structure, prohibiting the transmission coefficient to be recovered. Consequently, single waveguide probes only retrieve one out of the two scattering parameters (S-parameters), i.e., the reflection coefficient, in a measurement; hence, the use is convenient to determine the electromagnetic property, i.e., permittivity, of dielectric MUT. However, a magram demands both electromagnetic properties and therefore requires two independent reflection measurements.

1.2 Problem Statement

Two complex electromagnetic properties need to be determined for magRAM, and here, the MUT is assumed to be conductor-backed. A concept is desired in which two-independent reflection coefficients are retrieved during a measurement. Additionally, single waveguide probes have been proven to extract electromagnetic properties of materials, but the accuracy of the current techniques is limited by the accuracy of the theoretical model applied. Several single waveguide probe techniques have been studied and practiced to obtain the two necessary independent reflection measurements. Popular single waveguide probe techniques include the Dester et al., [3], Two-Thickness (TT) technique. The TT technique has dependable and accurate outcomes in obtaining the two reflection measurements. This technique involves measuring the reflection/transmission coefficients of two samples having two different known thickness.

Similarly, Stewart and Havrilla [4], characterize a conductor-backed lossy shielding material accomplished by using experimental reflection coefficients from two different thicknesses of the material. The theoretical reflection coefficients are obtained by using a rigorous magnetic field integral-equation formulation to extract the permittivity and permeability. As stated above, due to the theoretical model applied, these techniques are not applicable in all situations. This type of measurement can be useful in the laboratory because two samples of the MUT might be available and permanently affixed to a conductor backing. On the contrary, it is not practical in the field where the nature of the MUT is unknown. For example, some materials require *a priori* (knowing the electromagnetic properties prior to the experiment) of the MUT across frequencies to obtain the most agreeable results. A more viable technique is the Dester et al. [5], Two-Layer (TL) technique. The TL technique obtains the two independent reflection measurements. The first reflection measurement is collected by placing the probe against an unknown MUT. The second measurement is made when another known material is inserted between the probe and the unknown MUT. Due to relatively high error uncertainty results, the accuracy of this technique is limited.

Today, researchers are persistently trying to obtain an accurate and reliable technique for extracting the electromagnetic properties of conductor-backed magRAMs. In this effort, a measurement with and without an iris will be observed. Where the stepped-iris is a symmetrically reduced aperture in height which will be placed in front of conductor-backed magRAM using a rectangular waveguide. Anticipating that two independent reflection measurements arise. Ultimately, the goal of this research is to develop the stepped-iris technique for extracting the permittivity and permeability of magram.

1.3 Assumptions

The material samples are assumed to be simple media (linear, homogeneous, and isotropic). Additionally, it is assumed that the material is planar and uniform across the entire sample. Within the geometry, the PEC is assumed to be infinite in extent in the transverse direction and act as a perfect short circuit.

1.4 Scope

The measuring techniques discussed above may be used to extract the electromagnetic properties of the material, but in this thesis the only measurement technique that will be pursued is the single stepped-iris rectangular waveguide probe with a conductor-backed media. An exclusive measurement and analysis of a magram is examined. This measurement will only be considered as a proof-of-concept and validated through lab environment measurement; however, a waveguide probe technique can be used in the field after the knowledge of the electromagnetic fields transmitted through the material is determined reliable. Additionally, this thesis only considers the X-band (8-12.4 GHz) range of frequencies to evaluate the material.

1.5 Approach

The stepped-iris technique uses a single waveguide probe to determine permittivity and permeability of a material. A physical sample of the material will be provided and inserted into a rectangular waveguide component backed by a perfect electric conductor (PEC), coupled with and illuminated, in the X-band, by a Vector Network Analyzer (VNA). The first reflection measurement is obtained with the material backed by a PEC and inserted in the rectangular waveguide (with no waveguide stepped-iris). In the second measurement, a stepped-iris rectangular waveguide

is placed between the rectangular waveguide and the MUT. These measured reflection coefficients will then be entered into a MATLAB program devised to extract the the magram permittivity and permeability.The stepped-iris permittivity and permeability results are then compared to the permittivity and permeability computed via the well-known Nicholson-Ross-Weir (NRW) reflection/transmission technique. The stepped-iris technique is validated when its extracted permittivity and permeability matches the NRW results to within two standard deviations.

1.6 Material and Equipment

Resources required to complete this research include a calibration kit, 2-port VNA, rectangular waveguide components, computer/laptop, MATLAB application, and a FGM-125 material (magram). All equipment and components are available via the Microwave Laboratory located at AFIT.

1.7 Research Questions

The goal of this research is to answer two existing questions. Is there a technique that can acquire reliable and accurate electromagnetic properties from a conductor-backed absorbing material applying the mode matching approach to obtain the necessary theoretical reflection coefficients? Moreover, will a single stepped-iris be enough to alter the structure of the electromagnetic field to produce two independent reflection coefficients?

1.8 Thesis Overview

In Chapter 2, the rectangular waveguide theory will be reviewed, including the derivation of the the Helmholtz wave equation, followed by the separation of variables and ending with waveguide cut off frequencies. Chapter 3 provides the details of the

NRW and the stepped-iris material characterization technique. Chapter 4 discusses the process of the experiment, extracting the electromagnetic properties, the results and subsequent findings. Lastly, Chapter 5 ends the thesis with conclusions and recommendations for future work.

II. Background

2.1 Introduction

Chapter 2 provides the necessary background for the understanding of modal analysis that accommodates the resulting waveguide discontinuities in a rectangular waveguide with lossy media. In particular, field configurations (modes) of rectangular waveguides will be briefly reviewed through the construction of vector potentials.

2.1.1 Modes in rectangular waveguides.

Guided waves and waveguides were introduced around the late nineteenth century. Following this was the analysis of wave propagation leading into the theory and experimental knowledge, such as field configuration, in waveguide structures [6]. Generally, field configurations and their characteristics are supported and sustained by rectangular waveguide structures. Rectangular waveguide use increased circa World War II because of the development of microwave sources and amplifiers, such as magnetrons, klystrons, and traveling-wave tube amplifiers. The different bands influenced the standardized dimensions of rigid rectangular waveguides. Specifically, the most popular band used in communication was the standard X-band frequencies. These guides are popular since materials can be easily machined and fitted inside the cross-sectional plane of the waveguide; their unfailing durability and stability across low to high frequencies in retrieving electromagnetic properties; and they are available commercially off the shelf (COTS) and admit analytic closed form solutions.

To access an appropriate and unique solution to Maxwell's equations for practical application (i.e., involving material bodies with boundaries), it is required to understand the behavior of the electromagnetic field at the discontinuities (boundaries) separating material bodies with various electrical properties. General boundary-value

problems include standard waveguides structures that consist of various regions satisfying Maxwell's equations or the wave equation. However, this research effort examines a symmetrically reduced stepped-iris inserted between the rectangular waveguide structure and the media backed by perfect electrical conductor (PEC) in which the geometry encourages centering the origin in the middle of the rectangular waveguide, without loss of generality. A solution to this type of structure and electromagnetic boundary-value problem, that accommodates the resulting waveguide discontinuities, is conceivably expressed through field configurations that satisfy Maxwell equation's with the corresponding boundary conditions below.

A field configuration is derived of a particular mode for a given electromagnetic boundary-value problem. There are several modes that can exist in waveguide structures, but this review will only focus on the Transverse Electric (TE^z_{mn}) and Transverse Magnetic (TM^z_{mn}) modes where m and n are the modes, wavenumbers, inside the rectangular waveguide corresponding to the x and y, respectively. Most practical waveguide systems are designed to operate so that only the dominant TE_{10} propagating mode is excited, thus preventing the possibility of dispersion from higher-order modes propagating. In general, the mode with the lowest cutoff frequency is referred to as the "dominant mode." The interested reader can obtain more general review of modal analysis and waveguide theory from Collin and Balanis [6–8].

2.1.2 Helmholtz Wave equation.

Time harmonic fields (time variations of the form e^{jwt}) are the most common form used in practical time variation problems. In a linear, homogeneous and isotropic medium in regions where there are no sources, such as, $\mathbf{J}=\mathbf{M}=\mathbf{q}_{ev}=\mathbf{q}_{mv}=0$. Where $\mathbf{J}$ represents the electric current density, $\mathbf{M}$ represents the magnetic current density, $\mathbf{q}_e v$ represents electric charge density and $\mathbf{q}_m v$ represents the magnetic charge density.

All solutions in the time-harmonic field form must satisfy the following Maxwell equation's:

$$\nabla \times \mathbf{E} = -j\omega\mu\mathbf{H} \tag{1a}$$

$$\nabla \times \mathbf{H} = j\omega\varepsilon\mathbf{E} \tag{1b}$$

$$\nabla \cdot \mathbf{E} = 0 \tag{1c}$$

$$\nabla \cdot \mathbf{H} = 0 \tag{1d}$$

Where the electric field, $\mathbf{E}$, magnetic field, $\mathbf{H}$ represent the complex spatial forms of electromagnetic fields; angular frequency is represented by ω; and ε and μ represent the constitutive parameters permittivity and permeability, respectively [6, 7] .

The electromagnetic fields of boundary-valued problems are obtained as solutions to Maxwell's equations, which are first-order partial differential equations. However, the vector wave equation forms are generally preferred over the above Maxwell's equations because of its simple form. The solutions to the wave equation will be derived from the Maxwell's equations (1a), not in its entirety, in the subsequent paragraph. For more in depth derivation please refer to Balanis [7].

For the most part, when solving for $\mathbf{E}$, it is beneficial to uncouple the equation but at the expense of raising its order. To do this take the curl of both sides, using the vector identity where $\mathbf{G}$ is arbitrary

$$\nabla \times \nabla \times \mathbf{G} = \nabla(\nabla \cdot \mathbf{G}) - \nabla^2\mathbf{G}, \tag{2}$$

substituting the Maxwell's equation utilizing the constitutive relation and rearranging terms, we obtain the source-free vector wave equation

$$\nabla^2\mathbf{E} + k^2\mathbf{E} = 0 \tag{3}$$

where,

$$k^2 = \omega^2 \mu \varepsilon \tag{4}$$

Auxiliary vector potentials are a common practice in the analysis of electromagnetic boundary value problems. It is used as an aid in obtaining solutions for the electric and magnetic fields, **E** and **H**, respectively. Note that this may not illustrate clearly definable physical entities (i.e., absence of sources) and can be viewed as just useful as analytical functions from which the electromagnetic fields may be obtained. The most common vector potential functions are the **F**, electric vector potential and **A**, magnetic vector potential.

The principal type wave is a plane transverse electromagnetic wave (TEM). It is a wave, in which the electric and magnetic field vectors are in the plane that is transverse (perpendicular) to the propagation direction, the z-axis. However, this wave generally exists on an ideal transmission line, thus, other modes such as, transverse electric and magnetic, (TE) and (TM), respectively are considered in this review. The transverse electric field configurations (frequently illustrated as TE^z) are modes whose electric field components rest in the plane that is transverse to the wave propagation direction along the waveguide. Defined as TE to z direction (TE^z), this implies that E_z=0. Each of the other two electric field components (E_x and E_y) and three magnetic field components (H_x, H_y, and H_z) may or may not exist. The following solution will be demonstrated in the rectangular coordinate system [6, 7].

$$\mathbf{F}(x, y, z) = \hat{\boldsymbol{x}} F_x(x, y, z) + \hat{\boldsymbol{y}} F_y(x, y, z) + \hat{\boldsymbol{z}} F_z(x, y, z) \tag{5}$$

where x, y, z are the rectangular coordinates. Now, using the vector wave equation that was derived above, Eq. (5) can be substituted into Eq. (3). Subsequently, these

can be reduced to three scalar wave (Helmholtz) equations

$$\nabla^2 F_x(x,y,z) + k^2 F_x(x,y,z) = 0 \tag{6a}$$

$$\nabla^2 F_y(x,y,z) + k^2 F_y(x,y,z) = 0 \tag{6b}$$

$$\nabla^2 F_z(x,y,z) + k^2 F_z(x,y,z) = 0. \tag{6c}$$

TE^z electric and magnetic fields satisfy the specified equations:

$$\begin{aligned} E_x &= -\frac{1}{\varepsilon}\frac{\partial^2 F_z}{\partial y} & H_x &= -j\frac{1}{\omega\mu\varepsilon}\frac{\partial^2 F_z}{\partial x\ \partial z} \\ E_y &= \frac{1}{\varepsilon}\frac{\partial^2 F_z}{\partial x} & H_y &= -j\frac{1}{\omega\mu\varepsilon}\frac{\partial^2 F_z}{\partial y\ \partial z} \\ E_z &= 0 & H_x &= -j\frac{1}{\omega\mu\varepsilon}\Big(\frac{\partial^2}{\partial z^2} + k^2\Big)F_z \end{aligned} \tag{7}$$

where F_z(x,y,z) is a scalar potential function from Eq. (5) that represents the z component of the vector potential function **F**. The potential **F** must satisfy the Eq. (6c) which can be reduced to

$$\nabla^2 F_z + k^2 F_z = \frac{\partial^2 F_x}{\partial x^2} + \frac{\partial^2 F_x}{\partial y^2} + \frac{\partial^2 F_x}{\partial z^2} + k^2 F_z = 0. \tag{8}$$

2.1.3 Separation-of-Variables.

Using the separation-of-variables method, assume the solution for F_z(x,y,z) can be written in the form

$$F_z(x,y,z) = f(x)g(y)h(z) \tag{9}$$

where the x,y,z variation of F_z are separable. Substituting Eq. (8) into Eq. (9), leads to

$$gh\frac{\partial^2 f}{\partial x^2} + fh\frac{\partial^2 g}{\partial y^2} + fg\frac{\partial^2 h}{\partial z^2} + k^2 fgh = 0. \tag{10}$$

Dividing each term by fgh produces

$$\frac{1}{f}\underbrace{\frac{\partial^2 f}{\partial x^2}}_{-k_x^2} + \frac{1}{g}\underbrace{\frac{\partial^2 g}{\partial x^2}}_{-k_y^2} + \frac{1}{h}\underbrace{\frac{\partial^2 h}{\partial x^2}}_{-k_z^2} + k^2 = 0 \tag{11}$$

and the dispersion equation is written as

$$k_x^2 + k_y^2 + k_z^2 = k^2. \tag{12}$$

Because the waveguide is bounded in the x and y directions, the forms of $f(x)$ and $g(y)$ must be chosen to represent standing waves. Here $h(z)$ is represented as a traveling wave since the waveguide is infinite in length; thus,

$$f(x) = A\sin k_x(x + \tfrac{a}{2}) + B\cos k_x(x + \tfrac{a}{2}) \tag{13a}$$

$$g(y) = C\cos k_y(y + \tfrac{b}{2}) + D\sin k_y(y + \tfrac{b}{2}) \tag{13b}$$

$$h(z) = Ee^{-jk_z z} + Fe^{+jk_z z}. \tag{13c}$$

Substituting all three equations in Eq. (13) into Eq. (9), gives the result

$$\begin{aligned} F_z(x,y,z) = &\left[A\sin k_x(x + \tfrac{a}{2}) + B\cos k_x(x + \tfrac{a}{2})\right] \\ &\times \left[C\cos k_y(y + \tfrac{b}{2}) + D\sin k_y(y + \tfrac{b}{2})\right]\left[Ee^{-jk_z z} + Fe^{+jk_z z}\right] \end{aligned} \tag{14}$$

Recall, the tangential components of the electric field is zero ($E_{tang,z} = 0$), at the PEC waveguide walls. Below is the boundary conditions which leads to the permissible values of $k_{x,y}$ or called eigenvalues to achieve an unique solution

$$\begin{aligned} E_y(x = -\tfrac{a}{2}) = 0 \Rightarrow A = 0 \\ E_x(y = -\tfrac{b}{2}) = 0 \Rightarrow C = 0 \end{aligned} \tag{15}$$

$$\begin{aligned} E_y(x = \tfrac{a}{2}) = 0 \Rightarrow k_x = k_{xm} = \frac{m\pi}{a} \ldots m = 0, 1, 2, \ldots \\ E_x(y = \tfrac{b}{2}) = 0 \Rightarrow k_y = k_{yn} = \frac{n\pi}{b} \ldots m = 0, 1, 2, \ldots \end{aligned} \tag{16}$$

where m and n represent the designated modes (field configurations) for TE^z_{mn}, a and b represent the x and y direction on the rectangular waveguide, reference Fig. 1. Substituting Eq. (14) into Eq. (7) and writing the x and y components of the electric field produces the relations

$$\begin{aligned} E_x = -\frac{k_y}{\varepsilon}\big[A\sin k_x(x + \frac{a}{2}) + B\cos k_x(x + \frac{a}{2})\big] \\ \times \big[C\cos k_y(y + \frac{b}{2}) - D\sin k_y(y + \frac{b}{2})\big]\big[Ee^{-jk_z z} + Fe^{+jk_z z}\big] \end{aligned} \tag{17}$$

$$\begin{aligned} E_y = \tfrac{k_x}{\varepsilon}\big[A\cos k_x(x + \tfrac{a}{2}) - B\sin k_x(x + \tfrac{a}{2})\big] \\ \times \big[C\sin k_y(y + \tfrac{b}{2}) - D\cos k_y(y + \tfrac{b}{2})\big]\big[Ee^{-jk_z z} + Fe^{+jk_z z}\big]. \end{aligned} \tag{18}$$

After enforcing the bottom, top, right and left wall boundary conditions and if $BDE = \varepsilon A^+_{mn}$, $BDF = \varepsilon A^-_{mn}$ the F_z scalar function reduces to

$$F_{zmn} = \varepsilon\cos k_{xm}(x + \tfrac{a}{2})\cos k_{yn}(y + \tfrac{b}{2})\Big(A^+_{mn}e^{-jk_{zmn}z} + A^-_{mn}e^{+jk_{zmn}z}\Big). \tag{19}$$

In summary, the appropriate expression for TE^z_{mn} modes can be written as

$$E_{xmn} = k_{yn}\cos k_{xm}(x+\tfrac{a}{2})\sin k_{yn}(y+\tfrac{b}{2})\Big(A^+_{mn}e^{-jk_zz} + A^-_{mn}e^{+jk_zz}\Big) \tag{20a}$$

$$E_{ymn} = -k_{xm}\sin k_{xm}(x+\tfrac{a}{2})\sin k_{yn}(y+\tfrac{b}{2})\Big(A^+_{mn}e^{-jk_zz} + A^-_{mn}e^{+jk_zz}\Big) \tag{20b}$$

$$H_{xmn} = \frac{\frac{k_{xm}}{\omega\mu}}{k_{zmn}}\sin k_{xm}(x+\tfrac{a}{2})\sin k_{yn}(y+\tfrac{b}{2})\Big(A^+_{mn}e^{-jk_zz} - A^-_{mn}e^{+jk_zz}\Big) \tag{20c}$$

$$H_{ymn} = \frac{\frac{k_{yn}}{\omega\mu}}{k_{zmn}}\cos k_{xm}(x+\tfrac{a}{2})\sin k_{yn}(y+\tfrac{b}{2})\Big(A^+_{mn}e^{-jk_zz} - A^-_{mn}e^{+jk_zz}\Big) \tag{20d}$$

$$H_{zmn} = \frac{1}{j\omega\mu}(\underbrace{k^2 - k^2_{zmn}}_{k^2_{xm}+k^2_{yn}=k^2_{cmn}})\cos k_{xm}(x+\tfrac{a}{2})\sin k_{yn}(y+\tfrac{b}{2})$$
$$\Big(A^+_{mn}e^{-jk_zz} + A^-_{mn}e^{+jk_zz}\Big) \tag{20e}$$

where the wave impedance, from Eq. (20) shows that

$$Z^{TE}_{mn} = \frac{E_x}{H_y} = -\frac{E_y}{H_x} = \frac{\omega\mu}{k_{zmn}} \tag{21}$$

$\mathrm{Z}^{TE}_{mn} = \infty$ (open) and $\mathrm{Z}^{TM}_{mn} = 0$ (short) when $f = f_{cmn}$. The section below discusses f_{cmn} more in detail.

Note, that Transverse magnetic (TM) modes can be derived in a fashion similar to the TE fields where vector potential, **A**, has a nonvanishing component in the direction in which the TM fields are desired, and all the remaining components of **A** and **F** are set equal to zero [7, 9, 10].

2.1.4 Cutoff Frequency.

The demarcation separating the propagating and evanescent (nonpropagating) wave frequencies is usually referred to as the "cutoff," which occurs when

$$k_{zmn} = 0 \ldots \text{at cutoff.} \tag{22}$$

Stated in the Introduction section of Chapter 2, the mode with the lowest cutoff frequency is referred to as the dominant mode. This is when m=1 and n=0 (TE_{10}), a > b and

$$k = k_{cmn} \Rightarrow f_{cmn} = \frac{c}{2\sqrt{\epsilon_r \mu_r}} \sqrt{\frac{m^2}{a^2} + \frac{n^2}{b^2}} \tag{23}$$

where f_{cmn} is the cutoff frequency. To express the dominate mode and its largest bandwidth of a single-mode operation consider, for example in a free-space filled X-band waveguide with dimensions a = 0.02286 meters and b = 0.01016 meters here the cutoff frequency for the dominant TE_{10} mode is $f_{c10} = 6.561$ GHz, while that of the next higher-order mode, the TE_{20} mode, is $f_{c20} = 13.123$ GHz. X-band waveguides are traditionally operated in the frequency range $1.25 f_{c10} \leq f \leq 0.95 f_{c20}$ GHz which translate to $8.2 \leq f \leq 12.4$ GHz. This operational regime ensures a well-behaved dominant propagating mode with all higher-order modes being evanescent [7, 9].

2.2 Conclusion

The field configurations that occur inside a rectangular waveguide are subject to the dimensions of the waveguide, the medium filling the waveguide the cutoff frequencies of the various modes, and the coupling of energy from the source to the waveguide. Further, the wave propagation characteristics for waveguide structures can be determined, including their matching guide wavelengths, wave impedance, phase and attenuation constants. Assumptions and typical trends follow perfect in PEC walls, structures are vacuum filled, waveguide dimension (a =2b), and operational regimes fitting to best practices [6]. Consequently, the physical constraints however, forms other difficulties involving complex media, such as lossy media and terminated structures (probes, seen in Chapter 3). Best practice is to continue us-

ing the dominant mode to avoid excessive dispersion, but there are still obstacles in identifying and decoupling contributions of each individual propagating mode.

2.3 Summary

In this chapter a review of the modal-analysis technique derived utilizing the common auxiliary vector potentials expressed in TE^z and TM^z modes was discussed. Waveguide discontinuities were accommodated first through expanding the fields followed by separation of variable solution to the vector wave equation and enforcing boundary conditions across the waveguide structure. The existing fields inside the structure are the modes (field configurations). Subsequently, these modes can be used to analyze the discontinuities such as media and aperture in the structure. Chapter 3 will apply the modal-analysis technique discussed in Chapter 2 to three different waveguide structures including a standard structure with media, a structure conductor-backed media, and a structure with a stepped-iris placed in front of conductor-backed media; analyze the discontinuities (i.e., media and apertures) in each structure, and finally develop the stepped-iris technique to extract the materials electromagnetic properties.

III. Methodology

3.1 Introduction

The purpose of this research is to develop an extraction technique that can accurately and reliably characterize absorbing media for nondestructive (NDE) and noninvasive measurements of materials to assist visible and mechanical inspections. This chapter briefly provides a broad view of the stepped-iris extraction minimization algorithm and specifies a modal analysis process that derives the two theoretical reflection coefficients, $S_{11}^{thy,1}$ and $S_{11}^{thy,2}$, respectively which enables a method to extract the electromagnetic properties of a magnetic radar absorbing material (magRAM) sample in a conductor-backed and stepped-iris rectangular waveguide structure. The extracted electromagnetic properties are obtained via comparison of theoretical and experimentally measured scattering parameters estimated by a numerical root search algorithm.

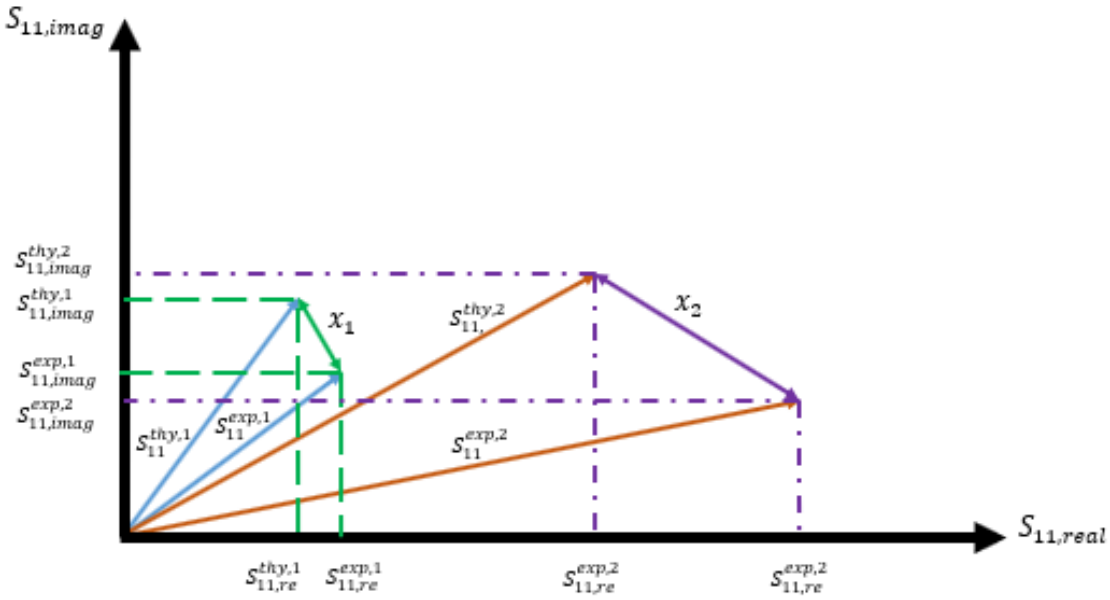

Figure 2. Decomposition of theoretical and experimental response is represented for case 1 (blue) and case 2 (orange) to estimate the most optimal ε_r and μ_r by determining the magnitude of the error between each response.

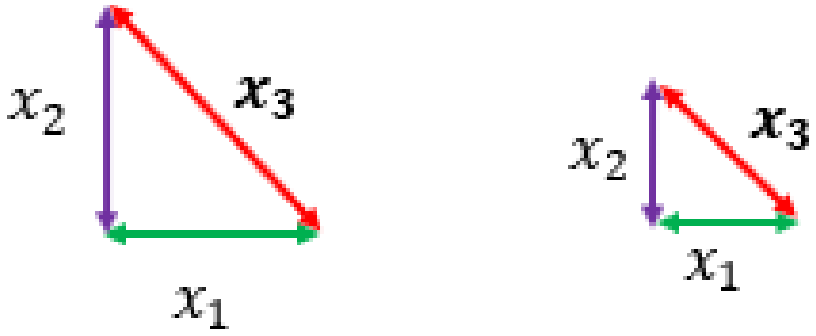

Figure 3. The minimization algorithms function is to minimize $x_3 \approx 0$ to produce the most optimal match between theoretical and experimental response.

3.2 Theory

Ultimately, the output from the stepped-iris extraction algorithm generates the optimal match between the theoretical and experimental response which conclusively represents the electromagnetic properties ε_r and μ_r, respectively. Above can be geometrically depicted in Figure 2 where both theoretical, S^{thy}, and experimental,S^{exp}, reflection coefficient vectors are decomposed onto $S_{11,re}$ and $S_{11,imag}$ plane. The error vector is the sum of squares between theoretical and experimental vector and is represented by x_i. The two norm mathematical measure of error in length leads to the result,

$$||x_i||_2 = \min_{\varepsilon_r,\mu_r \in \mathbb{C}} \left|\left| \sum_{i=1}^{2} S_{11}^{thy,i}(\omega,\varepsilon,\mu) - S_{11}^{exp,i}(\omega) \right|\right|_2 < \delta \tag{24}$$

where i is the number of measurements. Note, δ represents the termination tolerance on the function. In this effort, the Levenberg-Marquardt was utilized as the nonlinear least squares algorithm with a tolerance function, $\delta = 1 \times 10^{-7}$. The algorithm minimizes the error between theoretical and experimental reflection coefficients from both case 1 and case 2, x_1 and x_2, respectively where if the optimal match, x_3 goes to approximately zero, seen in Figure 3.

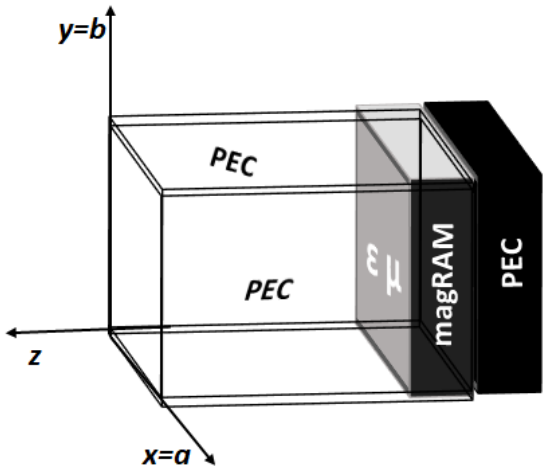

Figure 4. Conductor-backed Rectangular Waveguide. This hollow structure consist of four finite conducting walls with an open-end (side where the coordinates placed) and terminated by a perfect electric conductor (PEC (black)). The material under test (MUT) is inserted and completely filling the rectangular waveguide cross-section adjacent to the PEC. PEC does not allow transmission across interface; thus, only reflection measurements are measured.

3.3 Material and Equipment

Radar absorbers are widely used and are typically classified as impedance matching absorbers. These materials are customarily made from resistive and/or magnetic materials and fuse materials with different loss mechanisms. Typically, these materials make use of physical optics and combinations of many different shapes and structures to have robust absorption over wide bandwidths. In this paper, the Eccosorb FGM-125 material, magRAM shown Figure 4, is used to experimentally validate this proof-of-concept. It is thin, flexible, broadband silicone absorber and effective in reducing specular reflections as well as surface current traveling waves [11].

The Keysight (Agilent) E8362A Vector Network Analyzer (VNA), shown in Figure 5, will be used in this experiment to measure a magRAM sample in the frequency regime 8.2 - 12.4GHZ (i.e., X-band). The VNA has the combination of speed, precision and high-performance to test samples. The VNA also meets these testing

challenges by implementing the required sweep speeds, wide dynamic range, low trace noise and flexible connectivity. In addition, the VNA comes with Through-Reflection-Line (TRL) calibration for waveguide devices, 16 term error model, built-in hard drive and supplied mouse. The standard configuration used in the VNA measures linear components illuminated by a sweep. The following configuration can make either reflection measurements or transmission measurements, where only the reflection measurement will be utilized in this research effort. An incident signal generated by an Radio Frequency (RF) source controlled by the VNA is applied to the sample and compared with the signal reflected from the samples input [12].

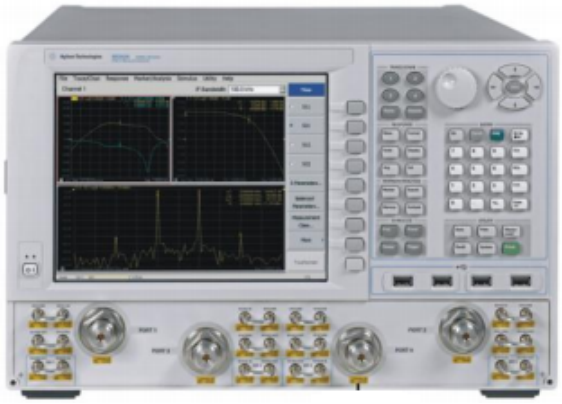

Figure 5. A photo of Keysight (Agilent) E8362A Vector Network Analyzer. 45 MHz to 40 GHz Vector Network Analyzer measures the magnitude and phase characteristics of electronic networks and other components such as filters, amplifiers, attenuators and antennas [12].

3.4 Procedure and Process

In this experiment, the procedure for developing an accurate and reliable extraction technique will be derived and modeled from the open-ended rectangular waveguide, discussed in Chapter 2, and Nicholson-Ross-Weir (NRW) material measurement technique. The open-ended rectangular structure has been used in past research and conventional material measurement techniques were developed to extract electromagnetic properties of material samples (i.e., NRW) [13] [14]. Nicholson-Ross-Wier(NRW) is well-known extraction method which extracts the electromagnetic properties of the media utilizing the experimentally measured S-parameters, S^{exp}, from the vector network analyzer and the reflection and transmission coefficients. These conventional techniques require a reflection measurement and a transmission coefficient to obtain the two independent equations needed to solve for the electromagnetic properties.

Usually, to apply the NRW technique, the sample must be simple media with parallel front and back surfaces and the material must fill the waveguide cross-section entirely [15]. However, if the material sample is permanently adhered to a conductor, then this technique cannot be used, due to the transmission coefficient not being

available.

In this effort, the material examined cannot have its conductor backing detached without affecting the electromagnetic properties, so in the next section a modal analysis method is presented to analyze theoretical reflection coefficient #1 denoted as $S_{11}^{thy,1}$ or Case 1 with a conductor-backed rectangular waveguide structure, completely filling its cross section, shown in Figure 4. Then, a modal analysis method is presented to analyze theoretical reflection coefficient #2 denoted as $S_{11}^{thy,2}$ or Case 2 with a symmetrically reduced stepped-iris in height (i.e. y-axis) along the waveguide dimension in x-axis, which restricts the conductor-backed material's upper and lower portion of illumination via VNA frequency sweep. Recall, modal analysis can be decomposed into three easy steps of expanding the electromagnetic fields in each region, satisfying boundary conditions across each interface/discontinuity, and testing by applying applicable integral operators. Consequently, these two reflection measurement coefficients serve the needed information to obtain the material's electromagnetic properties. Lastly, the extraction method in determining the material's electromagnetic properties (i.e. parameters) is discussed.

3.5 Method: Reflection Measurement #1

The side view of the conductor-backed geometry for the first reflection measurement is shown in Figure 6. The magRAM sample is placed in front of the PEC of the waveguide. Region A (z<0) is air-filled and Region B (z$\in (0, d)$) is the sample holder, sample contained inside, filling the entire rectangular cross-section having width d and height b. The PEC does not permit a transmission measurement.

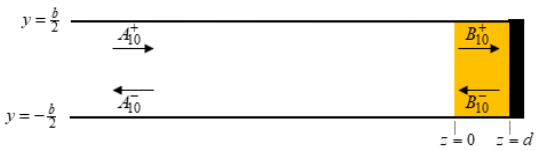

Figure 6. Reflection Measurement #1 diagram. This diagram is a side view of the conductor-backed rectangular waveguide. Divided into two regions A and B where each has a forward, +, and a reverse, -, traveling wave. Region A is air-filled and Region B (yellow) is the sample holder composed of the magRAM sample with a width d and a height b. In black, terminating the rectangular waveguide, represents a perfect electric conductor (PEC).

3.5.1 Field Expansion in Waveguide Regions.

The transverse fields in the waveguide regions (i.e., Regions A and B), are represented in the following expansions

$$\left.\begin{aligned}\mathbf{E}_t^A &= A_{10}^{+}\mathbf{e}_{t10}^A e^{-jk_{z10}^A z} + A_{10}^{-}\mathbf{e}_{t10}^A e^{jk_{z10}^A z}\\ \mathbf{H}_t^A &= A_{10}^{+}\mathbf{h}_{t10}^A e^{-jk_{z10}^A z} - A_{10}^{-}\mathbf{h}_{t10}^A e^{jk_{z10}^A z}\end{aligned}\right\} \quad \text{z<0} \tag{25}$$

$$\left.\begin{aligned}\mathbf{E}_t^B &= B_{10}^{+}\mathbf{e}_{t10}^B e^{-jk_{z10}^B z} + B_{10}^{-}\mathbf{e}_{t10}^B e^{jk_{z10}^B z}\\ \mathbf{H}_t^B &= B_{10}^{+}\mathbf{h}_{t10}^B e^{-jk_{z10}^B z} - B_{10}^{-}\mathbf{h}_{t10}^B e^{-jk_{z10}^B z}\end{aligned}\right\} \quad \text{z}\in(0,d) \tag{26}$$

where A_{10}^{+} represents the amplitude of the incident TE_{10} mode traveling in the positive z-direction, A_{10}^{-} represents the amplitude of the reflected TE_{10} mode from the waveguide to the sample holder interface at z=0. Similarly, B_{10}^{+} represents the amplitude of the transmitted TE_{10} mode through the sample region at z=0 and represents the amplitude of the incident mode at z=0, B_{10}^{-} represents the amplitude of the reflected TE_{10} mode from the sample holder to the waveguide region at interface at z=0, and the negative signs in magnetic field, $H_{10}^{A,B}$, equations represents the polarization rotation upon reflection. The other variables in the field expansions have the

following values for Regions A and B.

$$\mathbf{e}_{t10}^{A} = -\hat{y}k_{x1}\sin k_{x1}(x+\tfrac{a}{2}),\ k_{x1} = \frac{\pi}{a},\ \mathbf{h}_{10}^{A} = \frac{\hat{z}\times\mathbf{e}_{t10}^{A}}{Z_{10}^{A}}$$
$$Z_{10}^{A} = \frac{\omega\mu_0}{k_{z10}^{A}},\ k_{z10}^{A} = \sqrt{k_0^2 - k_{x1}^2} \tag{27}$$

$$\mathbf{e}_{t10}^{B} = \mathbf{e}_{t10}^{A},\ k_{x1} = \frac{\pi}{a},\ \mathbf{h}_{10}^{B} = \frac{\hat{z}\times\mathbf{e}_{t10}^{B}}{Z_{10}^{B}}$$
$$\mathbf{h}_{t10}^{B} = \frac{Z_{10}^{A}}{Z_{10}^{B}}\mathbf{h}_{t10}^{A}, Z_{10}^{A} = \frac{\omega\mu}{k_{z10}^{A}},\ k_{z10}^{B} = \sqrt{k^2 - k_{x1}^2}. \tag{28}$$

In this case (i.e., sample holder is the same dimension of the waveguide), the TE_{10} is the only mode needed to extract the material parameters since it is the only mode that exists.

3.5.2 Satisfying Boundary Conditions.

The next step in the modal analysis technique is to satisfy boundary conditions across each discontinuity and interface at $z = 0^{+,-}$ and $z = d$, (i.e., Region B) which leads to

$$\mathbf{E}_t^{B}(z=d) = 0 \Rightarrow B_{10}^{+}\mathbf{e}_{t10}^{B}\overbrace{e^{-jk_{z10}^{B}d}}^{P} + B_{10}^{-}\mathbf{e}_{t10}^{B}\overbrace{e^{jk_{z10}^{B}d}}^{P^{-1}}$$
$$\Rightarrow B_{10}^{-} = -B_{10}^{+}P^2 \tag{29}$$

where P represents the one way phase delay and attenuation in the forward traveling wave inside the material. Thus, enforcing continuity of tangential electric and

magnetic fields at z=0 leads to

$$\Rightarrow \begin{array}{l} \mathbf{E}_t^B = B_{10}^+ \mathbf{e}_{t10}^B e^{-jk_{z10}^B z}(1 - P^2 e^{j2k_{z10}^B z}) \\ \mathbf{H}_t^B = B_{10}^+ \mathbf{h}_{t10}^B e^{-jk_{z10}^B z}(1 + P^2 e^{j2k_{z10}^B z}) \end{array} \tag{30}$$

$$\mathbf{E}_t^A(z = 0^-) = \mathbf{E}_t^B(z = 0^+) \Rightarrow 1 + \underbrace{\frac{A_{10}^-}{A_{10}^+}}_{S_{11}^{thy}} = \underbrace{\frac{B_{10}^+}{A_{10}^+}}_{T}(1 - P^2)$$

$$\Rightarrow 1 + S_{11}^{thy} = T(1 - P^2) \tag{31}$$

$$\mathbf{H}_t^A(z = 0^-) = \mathbf{H}_t^B(z = 0^+) \Rightarrow 1 - S_{11}^{thy} = T\frac{Z_{10}^A}{Z_{10}^B}(1 + P^2), \tag{32}$$

where S_{11}^{thy} represents the theoretical reflection coefficient in the S-parameters and T represents the theoretical transmission coefficient at $z = 0$ interface. Dividing Eq. (31) by Eq. (32) produces the first reflection coefficient measurement:

$$\frac{1 + S_{11}^{thy}}{1 - S_{11}^{thy}} = \frac{T(1 - P^2)}{T\frac{Z_{10}^A}{Z_{10}^B}(1 + P^2)} \Rightarrow \boxed{S_{11}^{thy} = \frac{R - P^2}{1 - RP^2},\ R = \frac{Z_{10}^B - Z_{10}^A}{Z_{10}^B + Z_{10}^A}} \tag{33}$$

3.6 Method: Reflection Measurement #2

Figure 7 depicts the reduced stepped-iris conductor-backed rectangular waveguide. In this effort, the stepped-iris reduces the height, $y = h$, of the air-filled region, Region B, and the conductor-backed material rests behind the stepped-iris filling the entire cross section. In the past, step guides have been used to examine material

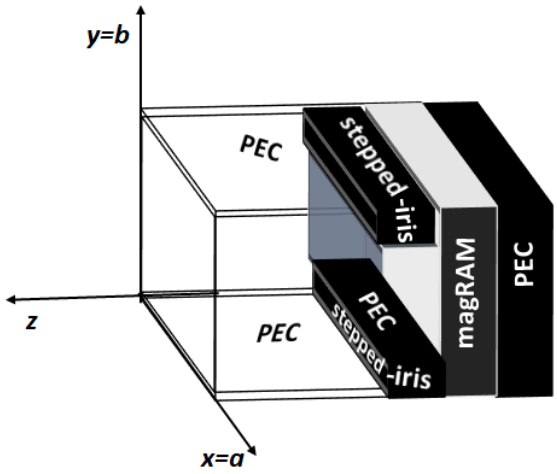

Figure 7. Stepped-iris conductor-backed Rectangular Waveguide. This hollow structure consist of four finite conducting walls with an open-end (side where the coordinates placed) and terminated by a perfect electric conductor (PEC (black)). The material under test (MUT) is inserted and completely filling the rectangular waveguide cross-section adjacent to the PEC. In addition, a stepped-iris is inserted in front of MUT (black). PEC does not allow transmission across interface, thus, only reflection measurements are measured only.

electromagnetic properties [16] [17]; however, in those cases the iris was horizontally reduced or a portion of the sample was fit into a vertically reduced stepped-iris, respectively.

The side view of the stepped-iris conductor-backed geometry for the second reflection measurement is shown in Figure 8. Note, excitation symmetry and scattering geometry forces the first index (x-variation) for the TE and TM modes to be "1" only and the second index (y-variation index) to be even (0,2,4,...). The k_z values for a given region and index values are the same for TE/TM modes. Region A ($z < 0$) is air-filled, Region B (z$\in$ $(0, \ell)$) is a symmetrically reduced stepped-iris (black) along the x-axis having width a and height $b - h$, the region between the stepped-iris is air-filled (green). The magRAM sample is in Region C, in front of the PEC (black) of the waveguide, $\ell < z < (\ell + d)$ filling the entire rectangular cross-section having width d and height b. The PEC does not permit a transmission measurement.

3.6.1 Field Expansion in Waveguide Regions.

An iris is a thin metal plate that forms discontinuities across the waveguide. This blockage or vertically reduced stepped-iris is placed in the transverse plane and works by exciting evanescent higher modes of both modes, TE and TM to z. However, the conventional waveguide configuration TE^z or TM^z modes alone cannot satisfy the boundary conditions of this structure, such as an empty waveguide with sample discussed above. Therefore, a separate and distinct mode configuration is developed to exist within this structure. Below presents the field configurations that are a combination of the two modes (i.e. TE^z and TM^z) that can be solutions and satisfy the boundary conditions of this structure.

The transverse fields in the waveguide regions are represented in the following expansions:

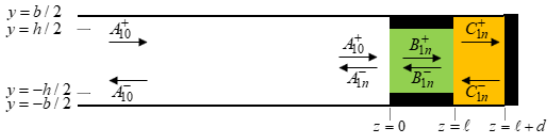

Figure 8. Reflection Measurement #2 diagram. This diagram is a side view of the stepped-iris conductor-backed rectangular waveguide. Divided into three regions A, B, and C where each has a forward, +, and a reverse, -, traveling wave. Region A is air-filled, reduced stepped-iris technique (black) in front of the material interface and Region B (green) air-filled, and Region C (yellow) is the sample holder composed of the magRAM sample with a width d and a height h < b.

Region A ($z < 0$)

$$\begin{aligned}
\mathbf{E}_t^A &= A_{1,0}^{+,TE}\mathbf{e}_{t1,0}^{A,TE}e^{-\gamma_{z1,0}^A z} + \sum_{n=1}^{N} A_{1,2(n-1)}^{-,TE}\mathbf{e}_{t1,2(n-1)}^{A,TE}e^{\gamma_{z1,2(n-1)}^A z} \\
&\quad + \sum_{n=2}^{N} A_{1,2(n-1)}^{-,TM}\mathbf{e}_{t1,2(n-1)}^{A,TM}e^{\gamma_{z1,2(n-1)}^A z} \\
\mathbf{H}_t^A &= A_{1,0}^{+,TE}\mathbf{h}_{t1,0}^{A,TE}e^{-\gamma_{z1,0}^A z} - \sum_{n=1}^{N} A_{1,2(n-1)}^{-,TE}\mathbf{h}_{t1,2(n-1)}^{A,TE}e^{\gamma_{z1,2(n-1)}^A z} \\
&\quad - \sum_{n=2}^{N} A_{1,2(n-1)}^{-,TM}\mathbf{h}_{t1,2(n-1)}^{A,TM}e^{\gamma_{z1,2(n-1)}^A z}
\end{aligned} \tag{34}$$

Region B ($0 < z < \ell$)

$$\begin{aligned}
\mathbf{E}_t^B &= \sum_{n=1}^{N} B_{1,2(n-1)}^{+,TE}\mathbf{e}_{t1,2(n-1)}^{B,TE}e^{-\gamma_{z1,2(n-1)}^B z} + \sum_{n=1}^{N} B_{1,2(n-1)}^{-,TE}\mathbf{e}_{t1,2(n-1)}^{B,TE}e^{\gamma_{z1,2(n-1)}^B z} \\
&\quad + \sum_{n=2}^{N} B_{1,2(n-1)}^{+,TM}\mathbf{e}_{t1,2(n-1)}^{B,TM}e^{-\gamma_{z1,2(n-1)}^B z} + \sum_{n=2}^{N} B_{1,2(n-1)}^{-,TM}\mathbf{e}_{t1,2(n-1)}^{B,TM}e^{\gamma_{z1,2(n-1)}^B z} \\
\mathbf{H}_t^B &= \sum_{n=1}^{N} B_{1,2(n-1)}^{+,TE}\mathbf{h}_{t1,2(n-1)}^{B,TE}e^{-\gamma_{z1,2(n-1)}^B z} - \sum_{n=1}^{N} B_{1,2(n-1)}^{-,TE}\mathbf{h}_{t1,2(n-1)}^{B,TE}e^{\gamma_{z1,2(n-1)}^B z} \\
&\quad + \sum_{n=2}^{N} B_{1,2(n-1)}^{+,TM}\mathbf{h}_{t1,2(n-1)}^{B,TM}e^{-\gamma_{z1,2(n-1)}^B z} - \sum_{n=2}^{N} B_{1,2(n-1)}^{-,TM}\mathbf{h}_{t1,2(n-1)}^{B,TM}e^{\gamma_{z1,2(n-1)}^B z}
\end{aligned} \tag{35}$$

Region C ($z > \ell$ to $z < \ell + d$)

$$\begin{aligned}
\mathbf{E}_t^C &= \sum_{n=1}^{N} C_{1,2(n-1)}^{+,TE}\mathbf{e}_{t1,2(n-1)}^{C,TE}e^{-\gamma_{z1,2(n-1)}^C (z-\ell)}\left[1 - P_{1,2(n-1)}^{C2}e^{2\gamma_{z1,2(n-1)}^C (z-\ell)}\right] \\
&\quad + \sum_{n=2}^{N} C_{1,2(n-1)}^{+,TM}\mathbf{e}_{t1,2(n-1)}^{C,TM}e^{-\gamma_{z1,2(n-1)}^C (z-\ell)}\left[1 - P_{1,2(n-1)}^{C2}e^{2\gamma_{z1,2(n-1)}^C (z-\ell)}\right] \\
\mathbf{H}_t^C &= \sum_{n=1}^{N} C_{1,2(n-1)}^{+,TE}\mathbf{h}_{t1,2(n-1)}^{C,TE}e^{-\gamma_{z1,2(n-1)}^C (z-\ell)}\left[1 + P_{1,2(n-1)}^{C2}e^{2\gamma_{z1,2(n-1)}^C (z-\ell)}\right] \\
&\quad + \sum_{n=2}^{N} C_{1,2(n-1)}^{+,TM}\mathbf{h}_{t1,2(n-1)}^{C,TM}e^{-\gamma_{z1,2(n-1)}^C (z-\ell}\left[1 + P_{1,2(n-1)}^{C2}e^{2\gamma_{z1,2(n-1)}^C (z-\ell)}\right]
\end{aligned} \tag{36}$$

where ℓ represents the length of the stepped-iris and air-filled Region B. The interested reader may locate the details in Appendix A to interpret Region C. Below is the indexing convention that corresponds to each Region, respectively

$$
\begin{aligned}
\mathbf{e}^{A,TE}_{1,2(n-1)} &= \hat{x}(-1)^n k^A_{y2(n-1)} \sin k_{x1}x \sin k^A_{y2(n-1)}y + \hat{y}(-1)^n k_{x1} \cos k_{x1}x \cos k^A_{y2(n-1)}y \\
\mathbf{e}^{A,TM}_{1,2(n-1)} &= \hat{x}(-1)^n k_{x1} \sin k_{x1}x \sin k^A_{y2(n-1)}y - \hat{y}(-1)^n k^A_{y2(n-1)} \cos k_{x1}x \cos k^A_{y2(n-1)}y \\
\mathbf{h}^{A,TE}_{t1,2(n-1)} &= \frac{\hat{z} \times \mathbf{e}^{A,TE}_{t1,2(n-1)}}{Z^{A,TE}_{1,2(n-1)}},\ \mathbf{h}^{A,TM}_{t1,2(n-1)} = \frac{\hat{z} \times \mathbf{e}^{A,TM}_{t1,2(n-1)}}{Z^{A,TM}_{1,2(n-1)}} \\
Z^{A,TE}_{1,2(n-1)} &= \frac{j\omega\mu_0}{\gamma^A_{z1,2(n-1)}},\ Z^{A,TM}_{1,2(n-1)} = \frac{\gamma^A_{z1,2(n-1)}}{\omega\varepsilon_0} \\
k_{x1} &= \frac{\pi}{a},\ k^A_{y2(n-1)} = \frac{2(n-1)\pi}{b},\ \gamma^A_{z1,2(n-1)} = \sqrt{k^2_{x1} + k^{A2}_{y2(n-1)} - k^2_0}
\end{aligned}
\tag{37}
$$

following a similar convention from Equations (27) and (28) where superscript A can be replaced with the B and C for each region. Note, in Region B the height is represented by h (See Appendix A). In addition, $m = 1$ and n even values which represents the different combinations that exist in that relative frequency range in both x and y directions, respectively.

3.6.2 Satisfying Boundary Conditions.

The next step in the modal analysis technique is to satisfy boundary conditions across each discontinuity and interface at $z = 0^{+,-}$, $z = \ell^{+,-}$ (i.e., Region B), and $z = \ell + d$ (note all BC's that follow are assumed valid in the region $0 < x < a$). Substituting the forward and backward wave propagation in Regions A, B, C and

dividing each field by A^{+}_{TE10} produces

$$\begin{aligned}
&\mathbf{R}^{A,TE}_{1,2(n-1)} = \tfrac{A^{-,TE}_{1,2(n-1)}}{A^{+,TE}_{1,0}} \ldots n = 1,\ldots,N,\ \mathbf{R}^{A,TM}_{1,2(n-1)} = \tfrac{A^{-,TM}_{1,2(n-1)}}{A^{+,TE}_{1,0}} \ldots n = 2,\ldots,N,\\
&\mathbf{R}^{B,TE}_{1,2(n-1)} = \tfrac{B^{-,TE}_{1,2(n-1)}}{A^{+,TE}_{1,0}} \ldots n = 1,\ldots,N,\ \mathbf{R}^{B,TM}_{1,2(n-1)} = \tfrac{B^{-,TM}_{1,2(n-1)}}{A^{+,TE}_{1,0}} \ldots n = 2,\ldots,N,\\
&\mathbf{T}^{B,TE}_{1,2(n-1)} = \tfrac{B^{+,TE}_{1,2(n-1)}}{A^{+,TE}_{1,0}} \ldots n = 1,\ldots,N,\ \mathbf{T}^{B,TM}_{1,2(n-1)} = \tfrac{B^{+,TM}_{1,2(n-1)}}{A^{+,TE}_{1,0}} \ldots n = 2,\ldots,N,\\
&\mathbf{T}^{C,TE}_{1,2(n-1)} = \tfrac{C^{+,TE}_{1,2(n-1)}}{A^{+,TE}_{1,0}} \ldots n = 1,\ldots,N, \mathbf{T}^{C,TM}_{1,2(n-1)} = \tfrac{C^{+,TM}_{1,2(n-1)}}{A^{+,TM}_{1,0}} \ldots n = 2,\ldots,N, \Rightarrow
\end{aligned} \tag{38}$$

where $\mathbf{R}$ and $\mathbf{T}$ are reflection and transmission coefficients, respectively. The superscript A, B, C correspond to each region.

Boundary Condition #1

$$\mathbf{E}^{A}_{t}(z=0^{-}) = \begin{cases} 0\ldots 0 < |y| > \frac{h}{2} \\ \mathbf{E}^{B}_{t}(z=0^{+})\ldots |y| < \frac{h}{2} \end{cases} \Rightarrow$$

$$\mathbf{e}^{A}_{t1,0} + \sum_{n=1}^{N} R^{A,TE}_{1,2(n-1)}\mathbf{e}^{A,TE}_{t1,2(n-1)} + \sum_{n=2}^{N} R^{A,TM}_{1,2(n-1)}\mathbf{e}^{A,TM}_{t1,2(n-1)} \tag{39}$$

$$= \begin{cases} 0\ldots |y| < \frac{h}{2} \\ \sum_{n=1}^{N} T^{B,TE}_{1,2(n-1)}\mathbf{e}^{B,TE}_{t1,2(n-1)} + \sum_{n=1}^{N} R^{B,TE}_{1,2(n-1)}\mathbf{e}^{B,TE}_{t1,2(n-1)} \\ + \sum_{n=2}^{N} T^{B,TM}_{1,2(n-1)}\mathbf{e}^{B,TM}_{t1,2(n-1)} + \sum_{n=2}^{N} R^{B,TM}_{1,2(n-1)}\mathbf{e}^{B,TM}_{t1,2(n-1)} \ldots |y| < \frac{h}{2} \end{cases}$$

Boundary Condition #2

$$\begin{aligned}
&\mathbf{H}_t^A(z=0^-) = \mathbf{H}_t^B(z=0^+) \ldots |y| < \tfrac{h}{2} \Rightarrow \\
&\mathbf{h}_{t1,0}^{A,TE} - \sum_{n=1}^{N} R_{1,2(n-1)}^{A,TE} \mathbf{h}_{t1,2(n-1)}^{A,TE} - \sum_{n=2}^{N} R_{1,2(n-1)}^{A,TM} \mathbf{h}_{t1,2(n-1)}^{A,TM} \\
&= \sum_{n=1}^{N} T_{1,2(n-1)}^{B,TE} \mathbf{h}_{t1,2(n-1)}^{B,TE} - \sum_{n=1}^{N} R_{1,2(n-1)}^{B,TE} \mathbf{h}_{t1,2(n-1)}^{B,TE} \\
&+ \sum_{n=2}^{N} T_{1,2(n-1)}^{B,TM} \mathbf{h}_{t1,2(n-1)}^{B,TM} - \sum_{n=2}^{N} R_{1,2(n-1)}^{B,TM} \mathbf{h}_{t1,2(n-1)}^{B,TM}
\end{aligned} \tag{40}$$

Boundary Condition #3 (note: $P_{1,2(n-1)}^{B} = e^{-\gamma_{z1,2(n-1)}^{B} \ell}$),

$$\mathbf{E}_t^C(z=\ell^+) = \begin{cases} 0 \ldots |y| > \frac{h}{2} \\ \mathbf{E}_t^B(z=\ell^-) \ldots |y| < \frac{h}{2} \end{cases} \Rightarrow$$

$$\sum_{n=1}^{N} T_{1,2(n-1)}^{C,TE} \mathbf{e}_{t1,2(n-1)}^{C,TE} \left[1 - P_{1,2(n-1)}^{C2}\right] + \sum_{n=2}^{N} T_{1,2(n-1)}^{C,TM} \mathbf{e}_{t1,2(n-1)}^{C,TM} \left[1 - P_{1,2(n-1)}^{C2}\right] \tag{41}$$

$$= \begin{cases} 0 \ldots |y| > \frac{h}{2} \\ \sum_{n=1}^{N} T_{1,2(n-1)}^{B,TE} \mathbf{e}_{t1,2(n-1)}^{B,TE} P_{1,2(n-1)}^{B} + \sum_{n=1}^{N} R_{1,2(n-1)}^{B,TE} \mathbf{e}_{t1,2(n-1)}^{B,TE} P_{1,2(n-1)}^{-1B} \\ + \sum_{n=2}^{N} T_{1,2(n-1)}^{B,TM} \mathbf{e}_{t1,2(n-1)}^{B,TM} P_{1,2(n-1)}^{B} + \sum_{n=2}^{N} R_{1,2(n-1)}^{B,TM} \mathbf{e}_{t1,2(n-1)}^{B,TM} P_{1,2(n-1)}^{-1B} \ldots |y| < \frac{h}{2} \end{cases}$$

Boundary Condition #4

$$\mathbf{H}_t^C(z=\ell^+)=\mathbf{H}_t^B(z=\ell^-)\ldots|y|<\tfrac{h}{2}\Rightarrow$$
$$\sum_{n=1}^{N}T_{1,2(n-1)}^{C,TE}\mathbf{h}_{t1,2(n-1)}^{C,TE}\left[1+P_{1,2(n-1)}^{C2}\right]+\sum_{n=2}^{N}T_{1,2(n-1)}^{C,TM}\mathbf{h}_{t1,2(n-1)}^{C,TM}\left[1+P_{1,2(n-1)}^{C2}\right] \tag{42}$$
$$=\sum_{n=1}^{N}T_{1,2(n-1)}^{B,TE}\mathbf{h}_{t1,2(n-1)}^{B,TE}P_{1,2(n-1)}^{B}-\sum_{n=1}^{N}R_{1,2(n-1)}^{B,TE}\mathbf{h}_{t1,2(n-1)}^{B,TE}P_{1,2(n-1)}^{-1B}$$
$$+\sum_{n=2}^{N}T_{1,2(n-1)}^{B,TM}\mathbf{h}_{t1,2(n-1)}^{B,TM}P_{1,2(n-1)}^{B}-\sum_{n=2}^{N}R_{1,2(n-1)}^{B,TM}\mathbf{h}_{t1,2(n-1)}^{B,TM}P_{1,2(n-1)}^{-1B}$$

Boundary Condition #5 (note, all BC's that follow are assumed valid in the region 0¡x¡a)

$$\mathbf{E}_t^C(z=\ell+d)=0\ldots0<y<b\Rightarrow$$
$$\sum_{n=1}^{N}C_{1,2(n-1)}^{+,TE}\mathbf{e}_{t1,2(n-1)}^{C,TE}\overbrace{e^{-\gamma_{z1,2(n-1)}^{C,TE}d}}^{P_{1,2(n-1)}^{C}}+\sum_{n=1}^{N}C_{1,2(n-1)}^{+,TE}\mathbf{e}_{t1,2(n-1)}^{C,TE}\overbrace{e^{\gamma_{z1,2(n-1)}^{C,TE}d}}^{P_{1,2(n-1)}^{-1C}}$$
$$+\sum_{n=1}^{N}C_{1,2(n-1)}^{-,TM}\mathbf{e}_{t1,2(n-1)}^{C,TM}\overbrace{e^{-\gamma_{z1,2(n-1)}^{C,TM}d}}^{P_{1,2(n-1)}^{C}}+\sum_{n=2}^{N}C_{1,2(n-1)}^{-,TM}\mathbf{e}_{t1,2(n-1)}^{C,TM}\overbrace{e^{\gamma_{z1,2(n-1)}^{C,TM}d}}^{P_{1,2(n-1)}^{-1C}}=0 \tag{43}$$

3.6.3 Testing with Integral Operators.

The last step of the modal analysis process applies testing operators on the boundary conditions enforced in the step above. Boundary condition enforcement reveals there will be 8 equations with 8N unknowns. To solve for these unknown coefficients it is necessary to apply 8N appropriate testing operators to generate 8N equations, which will lead to a 8N × 8N matrix, where $N = 1, 2, 3, \ldots, N$ is the quantity of

higher order modes. These modes $\mathbf{e}_{tTE1(n-1)}$, $\mathbf{h}^{TE}_{t1,2(n-1)}$, $\mathbf{e}^{TM}_{t1,2(n-1)}$, and $\mathbf{h}^{TM}_{t1,2(n-1)}$ will be appropriate testing function since these are used in this problem. Please refer to Appendix A for more detail.

Applying the testing operator $\int\limits_{CS_B} \mathbf{e}^{B,TE}_{t1,2(m-1)} \cdot \{\}\ ds \ldots m = 1, 2, 3, \ldots, N$ to (39) leads to the result

$$\overbrace{\int\limits_{CS_B} \mathbf{e}^{B,TE}_{t1,2(m-1)} \cdot \mathbf{e}^{A,TE}_{t1,0} ds}^{A_{m1}}$$
$$+ \sum_{n=1}^{N} \overbrace{\int\limits_{CS_B} \mathbf{e}^{B,TE}_{t1,2(m-1)} \cdot \mathbf{e}^{A,TE}_{t1,2(n-1)} ds}^{A_{mn}} R^{A,TE}_{1,2(n-1)} + \sum_{n=2}^{N} \overbrace{\int\limits_{CS_B} \mathbf{e}^{B,TE}_{t1,2(m-1)} \cdot \mathbf{e}^{A,TE}_{t1,2(n-1)} ds}^{B_{mn}} R^{A,TM}_{1,2(n-1)}$$
$$= \sum_{n=1}^{N} \overbrace{\int\limits_{CS_B} \mathbf{e}^{B,TE}_{t1,2(m-1)} \cdot \mathbf{e}^{B,TE}_{t1,2(n-1)} ds}^{C_{mn}} T^{B,TE}_{1,2(n-1)} + \sum_{n=1}^{N} \overbrace{\int\limits_{CS_B} \mathbf{e}^{B,TE}_{t1,2(m-1)} \cdot \mathbf{e}^{B,TE}_{t1,2(n-1)} ds}^{C_{mn}} R^{B,TE}_{1,2(n-1)}$$
$$+ \sum_{n=2}^{N} \overbrace{\int\limits_{CS_B} \mathbf{e}^{B,TE}_{t1,2(m-1)} \cdot \mathbf{e}^{B,TM}_{t1,2(n-1)} ds}^{0} T^{B,TM}_{1,2(n-1)} + \sum_{n=2}^{N} \overbrace{\int\limits_{CS_B} \mathbf{e}^{B,TE}_{t1,2(m-1)} \cdot \mathbf{e}^{B,TM}_{t1,2(n-1)} ds}^{0} R^{B,TM}_{1,2(n-1)} \Rightarrow \tag{44}$$

$$\sum_{n=1}^{N} A_{mn} R^{A,TE}_{1,2(n-1)} + \sum_{n=2}^{N} B_{mn} R^{A,TM}_{1,2(n-1)}$$
$$- \sum_{n=1}^{N} C_{mn} T^{B,TE}_{1,2(n-1)} - \sum_{n=1}^{N} C_{mn} R^{B,TE}_{1,2(n-1)} = -A_{m1} \ldots m = 1, \ldots, N \tag{45}$$

Applying the testing operator $\int\limits_{CS_B} \mathbf{e}^{B,TM}_{t1,2(m-1)} \cdot \{\}\ ds \ldots m = 2, 3, 4 \ldots, N$ to (39) leads to the result

$$\overbrace{\int\limits_{CS_B} \mathbf{e}^{B,TM}_{t1,2(m-1)} \cdot \mathbf{e}^{A,TE}_{t1,0} ds}^{D_{m1}}$$

$$+ \sum_{n=1}^{N} \overbrace{\int\limits_{CS_B} \mathbf{e}^{B,TM}_{t1,2(m-1)} \cdot \mathbf{e}^{A,TE}_{t1,2(n-1)} ds}^{D_{mn}} R^{A,TE}_{1,2(n-1)} + \sum_{n=2}^{N} \overbrace{\int\limits_{CS_B} \mathbf{e}^{B,TM}_{t1,2(m-1)} \cdot \mathbf{e}^{A,TM}_{t1,2(n-1)} ds}^{E_{mn}} R^{A,TM}_{1,2(n-1)}$$

$$= \sum_{n=2}^{N} \overbrace{\int\limits_{CS_B} \mathbf{e}^{B,TM}_{t1,2(m-1)} \cdot \mathbf{e}^{B,TE}_{t1,2(n-1)} ds}^{0} T^{B,TE}_{1,2(n-1)} + \sum_{n=1}^{N} \overbrace{\int\limits_{CS_B} \mathbf{e}^{B,TM}_{t1,2(m-1)} \cdot \mathbf{e}^{B,TE}_{t1,2(n-1)} ds}^{0} R^{B,TE}_{1,2(n-1)}$$

$$+ \sum_{n=2}^{N} \overbrace{\int\limits_{CS_B} \mathbf{e}^{B,TM}_{t1,2(m-1)} \cdot \mathbf{e}^{B,TM}_{t1,2(n-1)} ds}^{F_{mn}} T^{B,TM}_{1,2(n-1)} + \sum_{n=2}^{N} \overbrace{\int\limits_{CS_B} \mathbf{e}^{B,TM}_{t1,2(m-1)} \cdot \mathbf{e}^{B,TM}_{t1,2(n-1)} ds}^{F_{mn}} R^{B,TM}_{1,2(n-1)} \Rightarrow \tag{46}$$

$$\sum_{n=1}^{N} D_{mn} R^{A,TE}_{1,2(n-1)} + \sum_{n=2}^{N} E_{mn} R^{A,TM}_{1,2(n-1)} \tag{47}$$
$$- \sum_{n=2}^{N} F_{mn} T^{B,TM}_{1,2(n-1)} - \sum_{n=2}^{N} F_{mn} R^{B,TM}_{1,2(n-1)} = -D_{m1} \ldots m = 2, \ldots, N$$

Applying the testing operator $\int\limits_{CS_B} \mathbf{h}^{B,TE}_{t1,2(m-1)} \cdot \{\}\ ds \ldots m = 1, 2, 3, \ldots, N$ to (40) leads to the result

$$\overbrace{\int\limits_{CS_B} \mathbf{h}^{B,TE}_{t1,2(m-1)} \cdot \mathbf{h}^{A,TE}_{t1,0} ds}^{G_{m1}}$$

$$- \sum_{n=1}^{N} \overbrace{\int\limits_{CS_B} \mathbf{h}^{B,TE}_{t1,2(m-1)} \cdot \mathbf{h}^{A,TE}_{t1,2(n-1)} ds}^{G_{mn}} R^{A,TE}_{1,2(n-1)} - \sum_{n=2}^{N} \overbrace{\int\limits_{CS_B} \mathbf{h}^{B,TE}_{t1,2(m-1)} \cdot \mathbf{h}^{A,TM}_{t1,2(n-1)} ds}^{H_{mn}} R^{A,TM}_{1,2(n-1)}$$

$$= \sum_{n=1}^{N} \overbrace{\int\limits_{CS_B} \mathbf{h}^{B,TE}_{t1,2(m-1)} \cdot \mathbf{h}^{B,TE}_{t1,2(n-1)} ds}^{I_{mn}} T^{B,TE}_{1,2(n-1)} + \sum_{n=1}^{N} \overbrace{\int\limits_{CS_B} \mathbf{h}^{B,TE}_{t1,2(m-1)} \cdot \mathbf{h}^{B,TE}_{t1,2(n-1)} ds}^{I_{mn}} R^{B,TE}_{1,2(n-1)}$$

$$- \sum_{n=2}^{N} \overbrace{\int\limits_{CS_B} \mathbf{h}^{B,TE}_{t1,2(m-1)} \cdot \mathbf{h}^{B,TM}_{t1,2(n-1)} ds}^{0} T^{B,TM}_{1,2(n-1)} - \sum_{n=2}^{N} \overbrace{\int\limits_{CS_B} \mathbf{h}^{B,TE}_{t1,2(m-1)} \cdot \mathbf{h}^{B,TM}_{t1,2(n-1)} ds}^{0} R^{B,TM}_{1,2(n-1)} \Rightarrow \tag{48}$$

$$\sum_{n=1}^{N} G_{mn} R^{A,TE}_{1,2(n-1)} + \sum_{n=2}^{N} H_{mn} R^{A,TM}_{1,2(n-1)} + \sum_{n=1}^{N} I_{mn} T^{B,TE}_{1,2(n-1)} - \sum_{n=1}^{N} I_{mn} R^{B,TE}_{1,2(n-1)} = G_{m1} \ldots m = 1, \ldots, N \tag{49}$$

Applying the testing operator $\int\limits_{CS_B} \mathbf{h}^{B,TM}_{t1,2(m-1)} \cdot \{\}\ ds \ldots m = 2, 3, 4 \ldots, N$ to (40) leads to the result

$$\overbrace{\int\limits_{CS_B} \mathbf{h}^{B,TM}_{t1,2(m-1)} \cdot \mathbf{h}^{A,TE}_{t1,0} ds}^{J_{m1}}$$

$$- \sum_{n=1}^{N} \overbrace{\int\limits_{CS_B} \mathbf{h}^{B,TM}_{t1,2(m-1)} \cdot \mathbf{h}^{A,TE}_{t1,2(n-1)} ds}^{J_{mn}} R^{A,TE}_{1,2(n-1)} - \sum_{n=2}^{N} \overbrace{\int\limits_{CS_B} \mathbf{h}^{B,TM}_{t1,2(m-1)} \cdot \mathbf{h}^{A,TM}_{t1,2(n-1)} ds}^{K_{mn}} R^{A,TM}_{1,2(n-1)}$$

$$= \sum_{n=1}^{N} \overbrace{\int\limits_{CS_B} \mathbf{h}^{B,TM}_{t1,2(m-1)} \cdot \mathbf{h}^{B,TE}_{t1,2(n-1)} ds}^{0} T^{B,TE}_{1,2(n-1)} - \sum_{n=1}^{N} \overbrace{\int\limits_{CS_B} \mathbf{h}^{B,TM}_{t1,2(m-1)} \cdot \mathbf{h}^{B,TE}_{t1,2(n-1)} ds}^{0} R^{B,TE}_{1,2(n-1)}$$

$$+ \sum_{n=2}^{N} \overbrace{\int\limits_{CS_B} \mathbf{h}^{B,TM}_{t1,2(m-1)} \cdot \mathbf{h}^{B,TM}_{t1,2(n-1)} ds}^{L_{mn}} T^{B,TM}_{1,2(n-1)} - \sum_{n=2}^{N} \overbrace{\int\limits_{CS_B} \mathbf{h}^{B,TM}_{t1,2(m-1)} \cdot \mathbf{h}^{B,TM}_{t1,2(n-1)} ds}^{L_{mn}} R^{B,TM}_{1,2(n-1)} \Rightarrow \tag{50}$$

$$\begin{aligned} &\sum_{n=1}^{N} J_{mn} R^{A,TE}_{1,2(n-1)} + \sum_{n=2}^{N} K_{mn} R^{A,TM}_{1,2(n-1)} \\ &+ \sum_{n=2}^{N} L_{mn} T^{B,TM}_{1,2(n-1)} - \sum_{n=2}^{N} L_{mn} R^{B,TM}_{1,2(n-1)} = J_{m1} \ldots m = 2, \ldots, N \end{aligned} \tag{51}$$

Applying the testing operator $\int\limits_{CS_B} \mathbf{e}^{B,TE}_{t1,2(m-1)} \cdot \{\}\ ds \ldots m = 1, 2, 3, \ldots, N$ to (41) leads to the result

$$\sum_{n=1}^{N}\overbrace{\int_{CS_B}\mathbf{e}_{t1,2(m-1)}^{B,TE}\cdot\mathbf{e}_{t1,2(n-1)}^{C,TE}ds\big[1-P_{1,2(n-1)}^{C2}\big]}^{M_{mn}}T_{1,2(n-1)}^{C,TE}$$

$$+\sum_{n=2}^{N}\overbrace{\int_{CS_B}\mathbf{e}_{t1,2(m-1)}^{B,TE}\cdot\mathbf{e}_{t1,2(n-1)}^{C,TM}ds\big[1-P_{1,2(n-1)}^{C2}\big]}^{N_{mn}}T_{1,2(n-1)}^{C,TM}$$

$$=\sum_{n=1}^{N}\overbrace{\int_{CS_B}\mathbf{e}_{t1,2(m-1)}^{B,TE}\cdot\mathbf{e}_{t1,2(n-1)}^{B,TE}dsP_{1,2(n-1)}^{B}}^{O_{mn}}T_{1,2(n-1)}^{B,TE}$$

$$+\sum_{n=1}^{N}\overbrace{\int_{CS_B}\mathbf{e}_{t1,2(m-1)}^{B,TE}\cdot\mathbf{e}_{t1,2(n-1)}^{B,TE}dsP_{1,2(n-1)}^{-1B}}^{P_{mn}}R_{1,2(n-1)}^{B,TE}$$

$$+\sum_{n=2}^{N}\overbrace{\int_{CS_B}\mathbf{e}_{t1,2(m-1)}^{B,TE}\cdot\mathbf{e}_{t1,2(n-1)}^{B,TM}dsP_{1,2(n-1)}^{B}}^{0}T_{1,2(n-1)}^{B,TM}$$

$$+\sum_{n=2}^{N}\overbrace{\int_{CS_B}\mathbf{e}_{t1,2(m-1)}^{B,TE}\cdot\mathbf{e}_{t1,2(n-1)}^{B,TM}dsP_{1,2(n-1)}^{-1B}}^{0}R_{1,2(n-1)}^{B,TM}\Rightarrow \tag{52}$$

$$\sum_{n=1}^{N}M_{mn}T_{1,2(n-1)}^{C,TE}+\sum_{n=2}^{N}N_{mn}T_{1,2(n-1)}^{C,TM} \tag{53}$$
$$-\sum_{n=1}^{N}O_{mn}T_{1,2(n-1)}^{B,TE}-\sum_{n=1}^{N}P_{mn}R_{1,2(n-1)}^{B,TE}=0\ldots m=1,\ldots,N$$

Applying the testing operator $\int\limits_{CS_B}\mathbf{e}_{t1,2(m-1)}^{B,TM}\cdot\{\}\;ds\ldots m=2,3,4\ldots,N$ to (41) leads to the result

$$\sum_{n=1}^{N}\overbrace{\int\limits_{CS_B}\mathbf{e}_{t1,2(m-1)}^{B,TM}\cdot\mathbf{e}_{t1,2(n-1)}^{C,TE}ds\big[1-P_{1,2(n-1)}^{C2}\big]}^{Q_{mn}}T_{1,2(n-1)}^{C,TE}$$

$$+\sum_{n=2}^{N}\overbrace{\int\limits_{CS_B}\mathbf{e}_{t1,2(m-1)}^{B,TM}\cdot\mathbf{e}_{t1,2(n-1)}^{C,TM}ds\big[1-P_{1,2(n-1)}^{C2}\big]}^{R_{mn}}T_{1,2(n-1)}^{C,TM}$$

$$=\sum_{n=1}^{N}\overbrace{\int\limits_{CS_B}\mathbf{e}_{t1,2(m-1)}^{B,TM}\cdot\mathbf{e}_{t1,2(n-1)}^{B,TE}dsP_{1,2(n-1)}^{B}}^{0}T_{1,2(n-1)}^{B,TE}$$

$$+\sum_{n=1}^{N}\overbrace{\int\limits_{CS_B}\mathbf{e}_{t1,2(m-1)}^{B,TM}\cdot\mathbf{e}_{t1,2(n-1)}^{B,TE}dsP_{1,2(n-1)}^{-1B}}^{0}R_{1,2(n-1)}^{B,TE}$$

$$+\sum_{n=2}^{N}\overbrace{\int\limits_{CS_B}\mathbf{e}_{t1,2(m-1)}^{B,TM}\cdot\mathbf{e}_{t1,2(n-1)}^{B,TM}dsP_{1,2(n-1)}^{B}}^{S_{mn}}T_{1,2(n-1)}^{B,TM}$$

$$+\sum_{n=2}^{N}\overbrace{\int\limits_{CS_B}\mathbf{e}_{t1,2(m-1)}^{B,TM}\cdot\mathbf{e}_{t1,2(n-1)}^{B,TM}dsP_{TM1(n-1)}^{-1B}}^{T_{mn}}R_{1,2(n-1)}^{B,TM}\Rightarrow \tag{54}$$

$$\sum_{n=1}^{N}Q_{mn}T_{1,2(n-1)}^{C,TE}+\sum_{n=2}^{N}R_{mn}T_{1,2(n-1)}^{C,TM} \tag{55}$$
$$-\sum_{n=2}^{N}S_{mn}T_{1,2(n-1)}^{B,TM}-\sum_{n=2}^{N}T_{mn}R_{1,2(n-1)}^{B,TM}=0\ldots m=2,\ldots,N$$

Applying the testing operator $\int\limits_{CS_B}\mathbf{h}_{t1,2(m-1)}^{B,TE}\cdot\{\}\ ds\ldots m=1,2,3,\ldots,N$ to (42) leads to the result

$$\sum_{n=1}^{N} \overbrace{\int_{CS_B} \mathbf{h}_{t1,2(m-1)}^{B,TE} \cdot \mathbf{h}_{t1,2(n-1)}^{C,TE} ds\big[1 + P_{1,2(n-1)}^{C2}\big]}^{U_{mn}} T_{1,2(n-1)}^{C,TE}$$

$$+ \sum_{n=2}^{N} \overbrace{\int_{CS_B} \mathbf{h}_{t1,2(m-1)}^{B,TE} \cdot \mathbf{h}_{t1,2(n-1)}^{C,TM} ds\big[1 + P_{1,2(n-1)}^{C2}\big]}^{V_{mn}} T_{1,2(n-1)}^{C,TM}$$

$$= \sum_{n=1}^{N} \overbrace{\int_{CS_B} \mathbf{h}_{t1,2(m-1)}^{B,TE} \cdot \mathbf{h}_{t1,2(n-1)}^{B,TE} ds P_{1,2(n-1)}^{B}}^{W_{mn}} T_{1,2(n-1)}^{B,TE}$$

$$- \sum_{n=1}^{N} \overbrace{\int_{CS_B} \mathbf{h}_{t1,2(m-1)}^{B,TE} \cdot \mathbf{h}_{t1,2(n-1)}^{B,TE} ds P_{1,2(n-1)}^{-1B}}^{Xmn} R_{1,2(n-1)}^{B,TE}$$

$$+ \sum_{n=2}^{N} \overbrace{\int_{CS_B} \mathbf{h}_{t1,2(m-1)}^{B,TE} \cdot \mathbf{h}_{t1,2(n-1)}^{B,TE} ds P_{1,2(n-1)}^{B}}^{0} T_{1,2(n-1)}^{B,TM}$$

$$- \sum_{n=2}^{N} \overbrace{\int_{CS_B} \mathbf{h}_{t1,2(m-1)}^{B,TE} \cdot \mathbf{h}_{t1,2(n-1)}^{B,TM} ds P_{1,2(n-1)}^{-1B}}^{0} R_{1,2(n-1)}^{B,TM} \Rightarrow \tag{56}$$

$$\sum_{n=1}^{N} U_{mn} T_{1,2(n-1)}^{C,TE} + \sum_{n=2}^{N} V_{mn} T_{1,2(n-1)}^{C,TM} \tag{57}$$
$$- \sum_{n=1}^{N} W_{mn} T_{1,2(n-1)}^{B,TE} + \sum_{n=1}^{N} X_{mn} R_{1,2(n-1)}^{B,TE} = 0 \ldots m = 1, \ldots, N$$

Applying the testing operator $\int\limits_{CS_B} \mathbf{h}_{t1,2(m-1)}^{B,TM} \cdot \{\}\ ds \ldots m = 2, 3, 4 \ldots, N$ to (42) leads to the result

$$\sum_{n=1}^{N} \overbrace{\int_{CS_B} \mathbf{h}^{B,TM}_{t1,2(m-1)} \cdot \mathbf{h}^{C,TE}_{t1,2(n-1)} ds\big[1 + P^{C2}_{1,2(n-1)}\big]}^{Y_{mn}} T^{C,TE}_{1,2(n-1)}$$

$$+ \sum_{n=2}^{N} \overbrace{\int_{CS_B} \mathbf{h}^{B,TM}_{t1,2(m-1)} \cdot \mathbf{h}^{C,TM}_{t1,2(n-1)} ds\big[1 + P^{C2}_{1,2(n-1)}\big]}^{Z_{mn}} T^{C,TM}_{1(n-1)}$$

$$= \sum_{n=1}^{N} \overbrace{\int_{CS_B} \mathbf{h}^{B,TM}_{t1,2(m-1)} \cdot \mathbf{h}^{B,TE}_{t1,2(n-1)} ds P^{B}_{1,2(n-1)}}^{0} T^{B,TE}_{1,2(n-1)}$$

$$- \sum_{n=1}^{N} \overbrace{\int_{CS_B} \mathbf{h}^{B,TM}_{t1(m-1)} \cdot \mathbf{h}^{B,TE}_{t1,2(n-1)} ds P^{-1B}_{1,2(n-1)}}^{0} R^{B,TE}_{1,2(n-1)}$$

$$+ \sum_{n=2}^{N} \overbrace{\int_{CS_B} \mathbf{h}^{B,TM}_{t1,2(m-1)} \cdot \mathbf{h}^{B,TM}_{t1,2(n-1)} ds P^{B}_{1,2(n-1)}}^{\Gamma_{mn}} T^{B,TM}_{1,2(n-1)}$$

$$- \sum_{n=2}^{N} \overbrace{\int_{CS_B} \mathbf{h}^{B,TM}_{t1,2(m-1)} \cdot \mathbf{h}^{B,TM}_{t1,2(n-1)} ds P^{-1B}_{1,2(n-1)}}^{\Delta_{mn}} R^{B,TM}_{1,2(n-1)} \Rightarrow \tag{58}$$

$$\sum_{n=1}^{N} Y_{mn} T^{C,TE}_{1,2(n-1)} + \sum_{n=2}^{N} Z_{mn} T^{C,TM}_{1,2(n-1)} \tag{59}$$
$$- \sum_{n=2}^{N} \Gamma_{mn} T^{B,TM}_{1,2(n-1)} + \sum_{n=2}^{N} \Delta_{mn} R^{B,TM}_{1,2(n-1)} = 0 \ldots m = 2, \ldots, N$$

Now, arranging the coefficients in matrix form results in a $8N \times 8N$ matrix

$$\begin{bmatrix} A_{mn} & B_{mn} & -C_{mn} & 0 & -C_{mn} & 0 & 0 & 0 \\ D_{mn} & E_{mn} & 0 & -F_{mn} & 0 & -F_{mn} & 0 & 0 \\ G_{mn} & H_{mn} & I_{mn} & 0 & -I_{mn} & 0 & 0 & 0 \\ J_{mn} & K_{mn} & 0 & L_{mn} & 0 & -L_{mn} & 0 & 0 \\ 0 & 0 & -O_{mn} & 0 & -P_{mn} & 0 & M_{mn} & N_{mn} \\ 0 & 0 & 0 & -S_{mn} & 0 & -T_{mn} & Q_{mn} & R_{mn} \\ 0 & 0 & -W_{mn} & 0 & X_{mn} & 0 & U_{mn} & V_{mn} \\ 0 & 0 & 0 & -\Gamma_{mn} & 0 & \Delta_{mn} & Y_{mn} & Z_{mn} \end{bmatrix} \begin{bmatrix} R^{A}_{TE1(n-1)} \\ R^{A}_{TM1(n-1)} \\ T^{B}_{TE1(n-1)} \\ T^{B}_{TM1(n-1)} \\ R^{B}_{TE1(n-1)} \\ R^{B}_{TM1(n-1)} \\ T^{C}_{TE1(n-1)} \\ T^{C}_{TM1(n-1)} \end{bmatrix} = \begin{bmatrix} -A_{m1} \\ -D_{m1} \\ G_{m1} \\ J_{m1} \\ 0 \\ 0 \\ 0 \\ 0 \end{bmatrix} \tag{60}$$

where the set of all possible TE^{z}_{mn} and TM^{z}_{mn}, $m = 1, 2, 3, \ldots, N$ and $n = 0, 1, 2, \ldots, N$ is the column space of the matrix to the left, called matrix **A**. The column space of matrix **A** is the span of TE^{z}_{10} and higher order modes, $A_{mn}, B_{mn}, C_{mn}, etc, \ldots$, where N represents the quantity of higher order mode. The column space of matrix **A** is the range of the matrix transformation, **B**, $-A_{m1}, -D_{m1}, G_{m1}, etc.$ which represent the reflection and transmission coefficient from that region. Further, a linear combination of these vectors is any vector of the form,

$$R^{A,TE}_{1,2(n-1)} A_{mn} + \ldots T^{C,TE}_{1,2(n-1)} M_{mn} + \ldots \tag{61}$$

where R is the reflected coefficient from each region and T is the transmitted coefficient from each region represented in column vector by **x**. The column vector of matrix **A** can be written as a product of **A** with the column vectors, **x**. Therefore,

$\mathbf{Ax} = \mathbf{B}$ leads to the second reflection coefficient measurement

$$\mathbf{x} = \mathbf{A}/\mathbf{B} \tag{62}$$

$$\boxed{S_{11}^{(2)} = x_1(1,1)}$$

3.7 Material Parameter Extraction

To extract the electromagnetic properties at each frequency, a Newton's root-searching algorithm is used to find the electromagnetic properties that best match the theoretically calculated and experimentally measured S-parameters delineated in Eq. (24). The material parameter extraction technique used in this effort are performed by MatLAB. Note this algorithm has to represent all variables as real numbers. Thus, the complex electromagnetic properties are separated into real and imaginary parts,

$$||x_i|| = S_{11}^{thy,i} - S_{11}^{exp,i} = (S_{11}^{thy,i} - S_{11}^{exp,i}) - j(S_{11}^{thy,i} - S_{11}^{exp,i}) \tag{63}$$

where i is the number of cases. Reference Figure 2.

The modal analysis process outputs the theoretically calculated S-parameters, $S^{thy,i}$ $i = 1, 2$ (discussed above), used to predict the electromagnetic properties of the magRAM sample. Consequently, a root search algorithm generates the minimum value using an approximate initial guess inputted from the user of the magRAM sample's electromagnetic properties to match the theoretical calculated S-parameters and experimental values at each frequency, within a specified accuracy, namely

$$\begin{aligned} ||S_{11}^{thy,1}(\omega, \varepsilon, \mu) - S_{11}^{exp,1}(\omega)|| < \delta \\ ||S_{11}^{thy,2}(\omega, \varepsilon, \mu) - S_{11}^{exp,2}(\omega)|| < \delta. \end{aligned} \tag{64}$$

where 1 and 2 superscripts represent the theoretical and experimental reflection co-

efficient response from Case 1 and Case 2. Note, a typical value of $\delta = 1 \times 10^{-7}$.

3.8 Summary

A detailed description of magRAM material and VNA equipment was discussed and revealed the importance and difficulties in measuring and characterizing magRAM material. In addition, two methods were presented that accommodates the resulting wave discontinuities at the interfaces of a conductor-backed and stepped-iris rectangular waveguide structure, which utilized the three step modal analysis technique from the open-ended rectangular waveguide structure in Chapter 2. The electromagnetic boundary value problem was transformed into a matrix form for the theoretical S-parameters that predicted the electromagnetic properties. Lastly, a Newton's root search algorithm for extracting the magRAM samples electromagnetic properties from the experimental S-parameters was discussed.

IV. Measurement Uncertainty Analysis and Results

4.1 Introduction

Chapter 3 outlines an experimental method for a material extraction technique using an open-ended waveguide structure connected to two specific reflection cases that extend the physical insight for a successful *in situ* electromagnetic property extraction. The main goal of Chapter 4 is to compare the electromagnetic properties of the two independent theoretical reflection coefficients to the general NRW techniques using the developed stepped-iris extraction technique algorithm, discussed in Chapter 3, by measuring two materials in the X-band frequency (i.e. 8-12GHz). Specifically, experimental results for polymer material generally known as acrylic and magnetic radar absorbing material (magRAM) will be presented. Additionally, error analysis is applied to each technique to determine if the results are in agreement with one another.

The experimental setup will be addressed in the following section, but first an overview of sources of error in equipment, measurements and measurement uncertainties is discussed below. There are multiple potential sources of errors that arise with measurement error sources including, material under test (MUT) properties, systematic errors (i.e. Network Analyzer) and measurement uncertainties. Most of these categories listed can be negligible by ensuring the network analyzer is the following: properly constructed; proper measurement correction techniques used; and adequate MUT preparation is used coupled with material assumptions. However, the most important measurement uncertainty error to account for is from the electromagnetic material properties. Therefore, it is best practice to compute the uncertainty of the following: S-parameter measurements, air gaps, and sample position to ensure accurate results. The effects and discussions of systematic errors and VNA measurement

uncertainties will be examined in Section 4.2.1 in more detail.

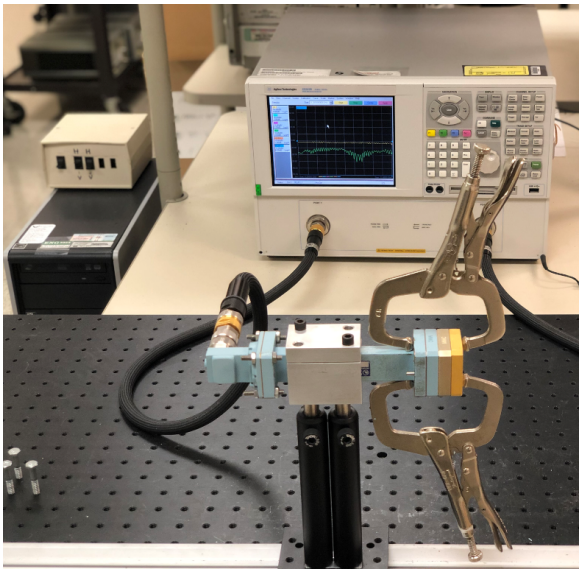

Figure 9. Experimental setup showing a WR90 waveguide connected to an E8362B Vector Network Analyzer with coaxial cables. The stepped-iris and conductor-backed sample holder is mounted to a single rectangular waveguide with alignment pins and clamps.

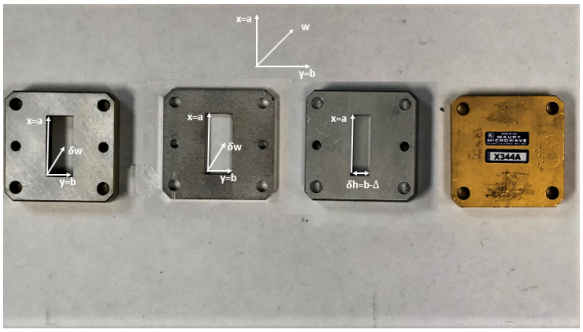

Figure 10. The first two on the left are full-aperture sample holders width, w=.01 and w=.0033 in meters, respectively, having the same dimension as rectangular waveguide. Third, is the stepped-iris reduced in height, h=.0071 in meters and width is the same dimension as the rectangular waveguide. Lastly, is a perfect electric conductor (PEC).

4.2 Experimental Setup

The experimental setup is shown in Figure 9 , the measured reflection coefficients $S_{11}^{meas1,2}$ were collected using an Agilent Technologies E8362B VNA in the X-band frequencies. A WR90 waveguide (i.e. abbreviation WR represents "waveguide rectangular" and 90 states the inner width a=.90 in. of the waveguide) where a=.02286 meters connected to the VNA via coaxial cables. Prior to the material measurements, the VNA was properly configured and calibrated. The cable junctions were cleaned with alcohol and junctions properly tightened with a torque wrench to ensure appropriate electrical contact. Also, the sample holder and attached stepped-iris were mounted to waveguide with alignment pins to minimize discontinuities at interfaces. Systematic error-terms were corrected by a full two-port *thru*, *reflect*, *line* (TRL) calibration procedure by measuring without the MUT using known calibration standards provided via VNA software and removing these effects from subsequent measurements.

4.2.1 Calibration Procedure.

The full two port process required to remove the effects of errors include the following *thru*, *reflect*, and *line* measurements. The VNA has two ports port 1 and port 2. Port 1 transmits/receives forward/reflected wave and port 2 receives transmitted waves from Port 1. These ports (i.e. port 1 and port 2) are connected to an open-ended WR90 extended from the VNA via the coaxial cable. The first measurement, *thru* is a measurement which port 1 and port 2 waveguides are aligned and connect with alignment pins and clamps with no line (i.e. sample holder). Second, *reflect* measurement consist of two measurements in which a brass plate (i.e. perfect electric conductor (PEC)) is clamped at the end of port 1. This measurement is repeated for port 2. Lastly, *line* measurement is a measurement which port 1 and

port 2 are aligned and connected with a line (i.e. sample holder) inserted between (i.e. port 1 and port 2) using alignment pins and clamps. The purpose of these three measurements is to remove the effect of errors from the VNA.

4.2.2 Measurement Procedure.

Next, the measurement process to measure the MUT at X-band frequencies is discussed. The only required port to measure the MUT is port 1 for reflection coefficient measurements. In this effort, the independent reflection measurements consist of two distinct cases described in Chapter 3, reflection measurement #1 (i.e. Case 1) and reflection measurement #2 (i.e. Case 2). The sample holder and the stepped-iris to verify the modal-analysis technique are shown in Figure 10. To minimize air gaps and alignment position between the sample holder and the conductor-back MUT clamps and alignment pins are used to connect the open-ended waveguide (i.e. port 1) . Reflection #1 measurement is a MUT conductor-backed connected to waveguide where the sample holder has the same dimensions of the waveguide. Reflection #2 measurement is a symmetrically reduced stepped-iris in height, conductor-backed MUT and sample holder(MUT inside) are connected to waveguide.

4.3 Error Analysis

The complex relative permittivity and permeability of the MUT will be estimated by finding Levenberg-Marquardt nonlinear least squares, which compared the theoretical reflection coefficient obtained from the modal analysis and the measured reflection coefficient obtained from the network analyzer at each frequency, within a specified accuracy of $\delta = 1 \times 10^{-7}$.

$$||x_i||_2 = \min_{\varepsilon_r, \mu_r \in \mathbb{C}} \left|\left| \sum_{i=1}^{2} S_{11}^{thy,i}(\omega, \varepsilon, \mu) - S_{11}^{exp,i}(\omega) \right|\right|_2 < \delta \tag{65}$$

where i is the number of iterations, S^{exp} represents the measured data, and S^{thy} represents the theoretical reflection response using the modal-analysis method. Errors when determining permittivity and permeability appear when the measured data has uncertainties in the S-parameters, from the VNA. As stated earlier other viable sources of error enter in from taking the measurement itself such as air gaps and sample position at the discontinuities. These types of errors can be eliminated by carefully aligning connecting parts with alignment pins and minimizing errors due to gaps with clamps. Another source of error is human error in measuring length and thicknesses of the stepped-iris, sample holder and sample respectively, which are inevitable and lead to the most difficult parameters to accommodate.

To observe the effects of errors and account for the measurement inaccuracy from the measurement uncertainties, a Taylor Series analysis was performed. In the analysis, error sources considered for evaluation were the following: material under test thickness d and a waveguide stepped-iris height h and length lsi. A uniform random variables distribution was applied to all measurement uncertainties.

The goal is to statistically quantify the effects and show how they influence the desired outputs. The desired outputs can be estimated as a function of material thickness d, stepped-iris height h, and length lsi approximated by the Talyor Series expansion. In this effort, the thickness and heights of the material and stepped-iris are relatively small values and become negligible when these higher order terms in the Taylor series expansion increases. Thus, the initial points of the measurements remains.

Independent perturbations can be conducted separately and then added together to determine the overall error from each specific uncertainty. The independent con-

tributions can be added in quadrature as

$$\sigma_{\varepsilon_r^{re}} = \sqrt{\left(\frac{\partial \varepsilon_r^{re}}{\partial d}\right)^2 \sigma_d^2 + \left(\frac{\partial \varepsilon_r^{re}}{\partial h}\right)^2 \sigma_h^2 + \left(\frac{\partial \varepsilon_r^{re}}{\partial lsi}\right)^2 \sigma_{lsi}^2} \tag{66}$$

where $\sigma_{\varepsilon_r^{re}}$, is the standard deviation of real relative permittivity. Thus, the best estimate of $\sigma_{\varepsilon_r^{re}} = \varepsilon_r^{re}(d_o, h_o, lsi_o) \pm k\sigma_{\varepsilon_r^{re}}$, where $k = 1, 2, 3, \ldots$ which correspond to a higher percentile of standard deviation. Note each electromagnetic property can be determined in similar manner. For a more information the reader can refer to NIST Technical Note 1355-R [18]

4.4 Results

The comparison of the stepped-iris extraction technique with the NRW technique was provided by experimentally measuring polymer and ECCOSORB FGM-125 representing a dielectric material and magnetic radar absorbing material (magRAM), respectively, in the X-band frequency (i.e. 8.2-12.4GHz) to obtain the electromagnetic properties of the material. Case 1 and Case 2 only used the acrylic material by assuming the μ=1 of the material. Case 3 merges the two Cases to obtain ε and μ. These three Cases demonstrates the accuracy and reliability of this technique. In addition, it is shown that higher-order modes are not significant to converge.

4.4.1 Case 1.

Initially, a biaxial acrylic sample filling the entire length of the sample was measured using the modal-analysis technique as a preliminary model. Note, due to the class of material consistent measurements were taken where the biaxial acrylic material was oriented and measured in the y direction only, thus fitting the isotropic dielectric characteristics needed to support this extraction technique. Acrylic material has a rigid structure and displays low dielectric loss, nondispersive, relatively low

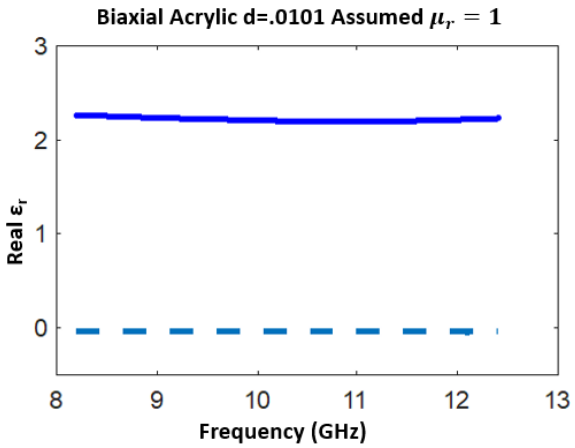

Figure 11. Extraction permittivity using root-search algorithm from conductor-backed biaxial acrylic material completely filling full-aperture sample holder mounted to single rectangular waveguide (No stepped-iris).

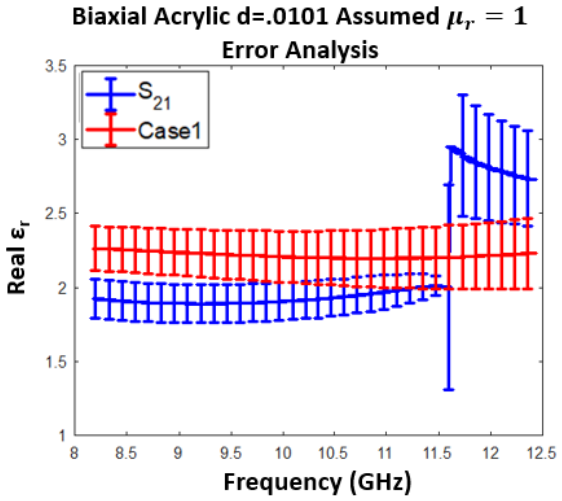

Figure 12. Permittivity compared between Case 1 and S_{21} Transmission only measurement convergence with just 1 mode.

dielectric constant and non-magnetic properties analogous to pure dielectric characteristics. Further, having *a priori* knowledge of the sample and its desirable qualities acrylic makes this an ideal material to check this material extraction technique by using its permittivity property. The electromagnetic properties of the acrylic sample (ε_r=2.31 and μ_r=1) were determined using the Nicolson, Ross, Weir (NRW) method.

Experimentally, this measurement was without the stepped-iris and used the sample holder (far left) and the short (far right) in Figure 10 and the theoretical response used the modal analysis to determine the reflection coefficient. Case 1 extraction root-search algorithm was utilized to extract the permittivity parameter, seen in Figure 11. The extracted permittivity and the assumed permeability convergence of mode 1 compared to the S_{21} transmission are shown in Figure 12. With an initial guess of ε=2.33 the complex permittivity are an accurate extraction and is a near perfect comparison. An explanation not seen physically in the graphic is the root-search algorithm reliability and accuracy obtaining the permittivity of the acrylic material. Deliberately providing the algorithm a $+/-3.5$ initial input guess from by the user the obtained ε parameter still converges with only 1 mode.

4.4.2 Case 2.

Case 2 measures the biaxial acrylic material with the stepped-iris placed in front with the hopes of sufficiently retrieving another independent measurement of the electromagnetic properties of the material. The stepped-iris inner dimensions were w=.0097 meters and h=.0071 meters. The biaxial acrylic material filled the entire aperture of the sample holder d=.0101 meters. In Figure 10, sample holder (far left), stepped-iris (second to far right) and short (far right) were used experimentally. Case 2 stepped-iris extraction technique is similarly used as in Case 1 one to obtain the electromagnetic properties.

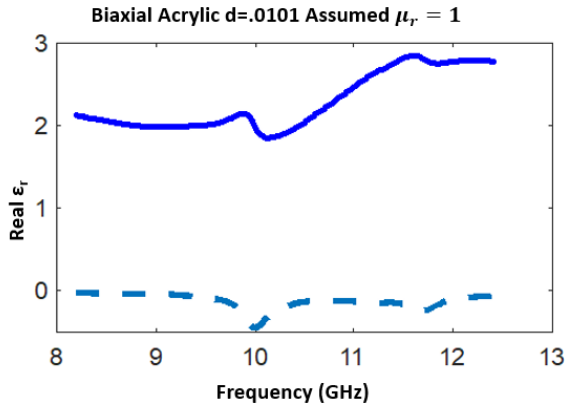

Figure 13. Extraction of complex permittivity using root-search algorithm from conductor-backed biaxial acrylic material completely filling full-aperture sample holder mounted to single rectangular waveguide with stepped-iris inserted between rectangular waveguide and sample holder. Complex permittivity properties are excited in the stepped-iris region from the reduced height.

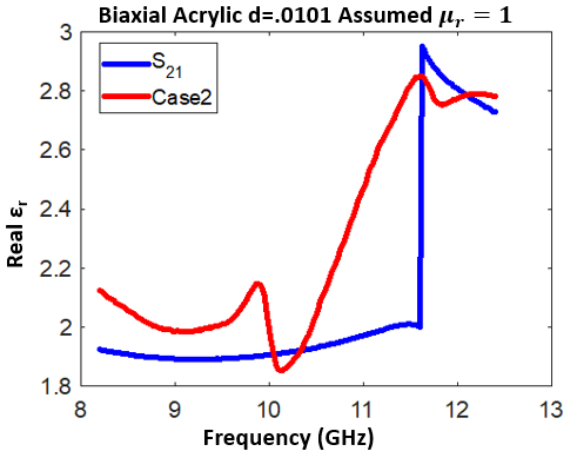

Figure 14. Comparison between real permittivity in NRW and Case 2 material extraction technique. Note, Acrylic is a dielectric material with nonmagnetic properties, assuming $\mu_r = 1$.

Indeed, an independent measurement is achieved obtaining the ε parameter while assuming that μ=1. The Figure 13 corroborates this claim, it appears to be perturbations involved with inserting the symmetrically reduced height stepped-iris in the y-axis along the x-axis. This physical insight implies that the incident wave, A_{10}^{TE} is excited on the stepped-iris region (i.e. Region B, z=0) from Region A, and reflected back into Region A interfering continued transmitting waves from Region A. Additionally, the transmitted wave passing through the stepped-iris region Region B (i.e. Region B, z=0) gets excited once again entering sample holder and material region (i.e. Region C, z=l), creating yet another reflection back to Region A. The reflected wave travels through Region B, therefore concluding the infinitely higher-order modes play a huge part in perturbing the fields adequately to provide an independent reflection measurement. Another look comparing the NRW measurement and Case 2 using the biaxial acrylic is shown in Figure 14.

4.4.3 Case 3.

Case 3 needs to obtain the two unknowns, both permittivity and permeability, utilizing two equations. This is accomplished by combining Case 1 and Case 2 (i.e. two equations) together where each cases uses the Levenberg-Marquardt nonlinear

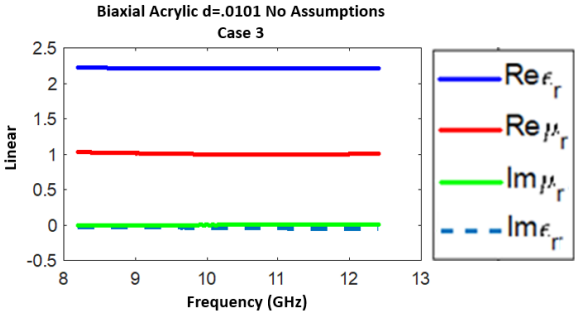

Figure 15. Extraction of complex permittivity and permeability using root-search algorithm from Case 1 and Case 2 between theoretical and measurement reflection response, without and with stepped-iris, respectively.

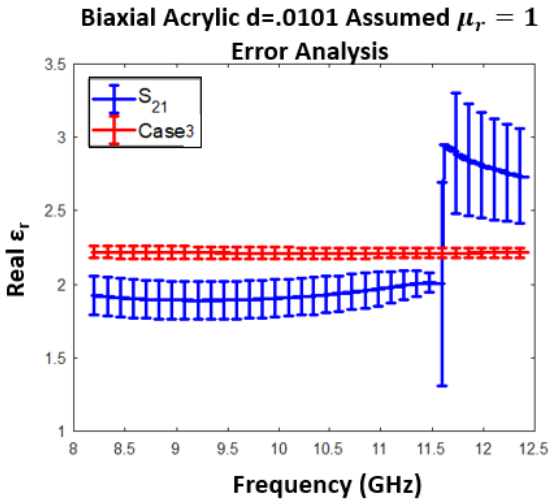

Figure 16. Permittivity compared between Case 3 and S_{21} Transmission only measurement convergence with just 1 mode. Conductor-backed media improves permittivity measurement by eliminating half resonance developed from thick material.

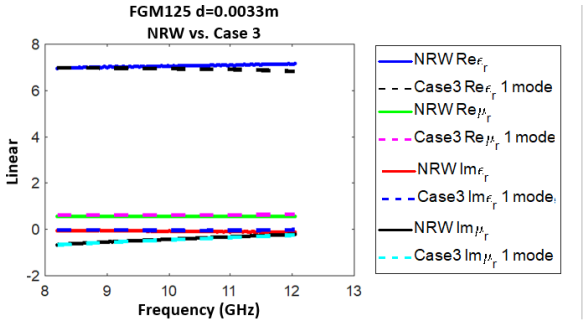

Figure 17. Extraction of complex permittivity and permeability using root-search algorithm from from Case 1 and Case 2 between theoretical and measurement reflection response, without and with stepped-iris, respectively, with just 1 mode.

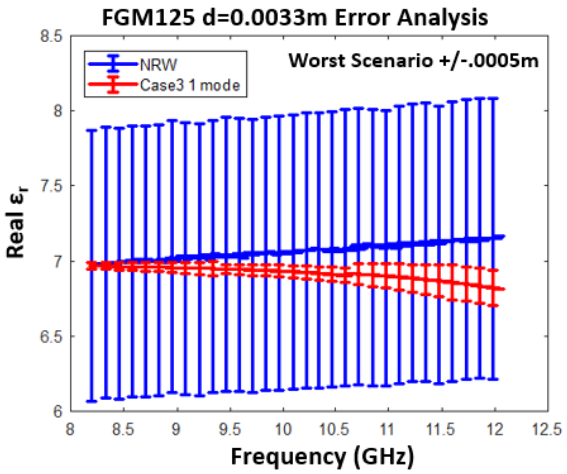

Figure 18. Permittivity convergence of 1 mode to classical NRW method within 95% confidence. Near exact, but small deviation due to measurement uncertainties and less significant electric field presence from conductor-backing.

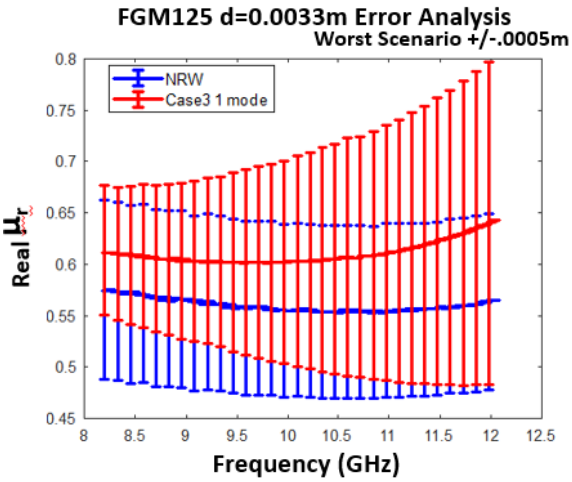

Figure 19. Permeability convergence of 1 mode to classical NRW method.Near exact, but sensitivity increased due to strong magnetic field existence at conductor-backing.

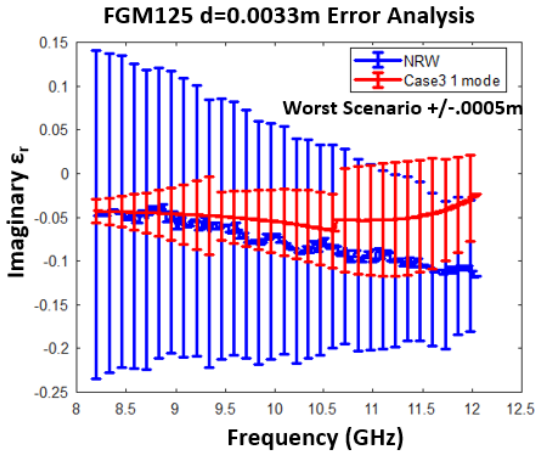

Figure 20. Permittivity convergence of 1 mode to classical NRW method within 95% confidence. Near exact, but small deviation due to measurement uncertainties and less significant electric field presence from conductor-backing.

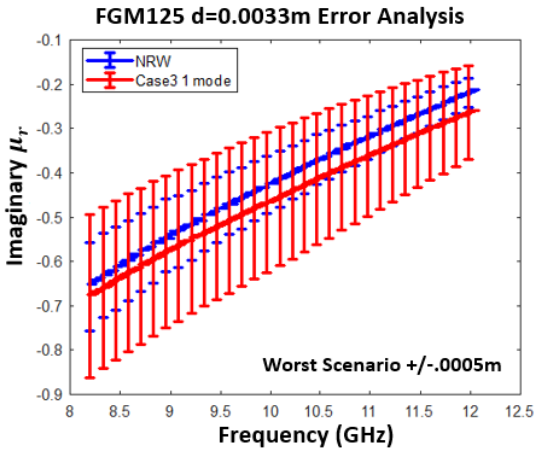

Figure 21. Permeability convergence of 1 mode to classical NRW method.Near exact, but sensitivity increased due to strong magnetic field existence at conductor-backing.

least squares algorithm to find the optimal match between the theoretical reflection response and experimental reflection coefficient at each frequency, respectively. Ultimately, the output of each optimal match represents the extracted permittivity and permeability of the material with making no assumption of any electromagnetic property. Reference Chapter 3 for more detail.

Figure 15 is the extracted electromagnetic properties of a biaxial acrylic material. These results suggest that the developed stepped-iris technique favorably represents the electromagnetic properties of dielectric material. Figure 16 depicts the comparison between permittivity obtained using the stepped-iris extraction technique of the biaxial acrylic material, aligning slightly atop of the S_{21} transmission only from the NRW technique. The typical transmission and reflection coefficient NRW extraction technique cannot be used to compare because the thickness of the material develops a half resonance which provides another benefit to the stepped-iris extraction technique. It appears using a conductor-backed media eliminates half resonance in thicker materials indicated from the permittivity agreeing with the S_{21} transmission data from NRW. Experimentally, dielectric material in Case 3 extraction technique seems to converge with the NRW technique with 1 mode, thus with agreeable data leads to the anticipation of the stepped-iris extraction techniques effectiveness with magRAM material. Now, the following will discuss the results for the magRAM material and comparing the obtained complex electromagnetic property to the classical NRW method.

MagRAM electromagnetic properties are more difficult since both ε and μ have real and imaginary values, rather than being able to assume that μ=1 as for dielectric material. FMG-125 represents the magRAM MUT and the sample holder used in this experiment can be viewed in Figures 10. The FGM-125 material was cut from a sheet of Eccosorb FGM-125 just slightly larger than the sample holder to minimize

as much space and gaps as possible. Both the sample and the sample holder were approximately d=.0033 meters wide.

The result shows that in fact it resoundingly exhibits convergence with the classical NRW method for FGM-125 electromagnetic properties. The permittivity is seen to be in almost perfect agreement with the NRW results, shown in Figure 17.

In addition, the material is conductor-backed by which perhaps leads to the insensitive permittivity output since the E_t=0 on a PEC, thus not strongly affecting permittivity, shown in Figure 18. On the contrary, the magnetic field is considerably stronger at the conductor-backed PEC, leading to the complex permeability values near exact to the classical NRW method seen in Figure 19. The imaginary permittivity is within 2σ standard deviation with NRW technique, seen in Figure 20 and imaginary permeability agrees with NRW technique as well, shown in Figure 21 which both seem to change in correlation to the real part from the higher-order modes introduced. Moreover, convergence was established using 1 mode and other contributions imperfections are due from either the uncertainty in the S-parameter, material length and gaps.

The physical insight beautifully agrees between the theoretical response and measurement data verifying that a symmetrically reduced height stepped-iris influences enough perturbations inside the structure to produce a sufficiently independent measurement to obtain the electromagnetic properties of a magRAM material.

4.5 Summary

Both Biaxial acrylic and FGM-125 materials were measured in two independent reflection cases to validate the stepped-iris extraction technique. The biaxial acrylic material was shown for Case 1 and Case 2 due to the known permeability for a dielectric material. Case 1 results matched the material's properties extremely well

when compared to NRW method. Case 2 shows that indeed the reduced stepped-iris in height perturbs the electric field enough to produce an independent reflection coefficient. Lastly, FGM-125 compared with NRW method results were statistically excellent. Convergence with the use just of 1 mode demonstrates that this technique is reliable for obtaining the electromagnetic properties of a conductor-backed media.

V. Conclusions and Recommendations

In this paper, a new single stepped-iris waveguide extraction technique was presented to nondestructively determine the permittivity and permeability of conductor-backed media. A full-wave solution combined with a mode matching method which accommodates the resulting waveguide structure's discontinuities across the various interfaces was implemented. The performance of this extraction technique was estimated by firstly, finding Levenberg-Marquardt nonlinear least squares, which compared the theoretical reflection coefficient obtained from the modal analysis and the measured reflection coefficient obtained from the network analyzer at each frequency, within a specified accuracy of $\delta = 1\times\ 10^{-7}$. Secondly, performing and conducting a Taylor Series analysis on the stepped-iris extraction technique which accommodates the physical measurement uncertainties when compared to the Nicolson-Ross-Weir (NRW) electromagnetic property measurements of each material.

The comparison of the stepped-iris extraction technique with the NRW technique was provided by experimentally measuring polymer and ECCOSORB FGM-125 representing a dielectric material and magnetic radar absorbing material (magRAM), respectively, in the X-band frequency (i.e. 8.2-12.4GHz). The three cases demonstrated a notably accurate, reliable and concluding that this technique agrees favorably with the NRW technique, thus proving that stepping the waveguide in the y-axis symmetrically along the x-axis indeed perturbs the field sufficiently to obtain the electromagnetic properties of the material. In addition, the physical insight revealed that permittivity is not sensitive due to electric field being zero at the PEC, thus, permeability parameters are more sensitive since the magnetic field is maximum at the PEC which explains its close agreement to the NRW method.

The Taylor Series analysis supports the physical insight with convergence within the classical NRW method error bars under 1 mode. Moreover, no higher-order modes

such as the $TE_{1,2(n-1)}$ are required in this scenario, suggesting that the stepped-iris excites higher-order modes, but vanish before making any significant contribution to effectively accommodate the medium inside the rectangular waveguide. Nonetheless, this enables *in situ* measurements in obtaining electromagnetic properties of conductor-backed magRAM material using a stepped-iris rectangular waveguide.

5.1 Future Work

Focus in accurately and reliably characterizing magnetic radar absorbing material experimentally in the X-band operating frequencies has been expanding, especially in search for an effective technique. Although, in this effort, the stepped-iris extraction technique was in favor, additional application in this technique can further augment the stepped-iris extraction technique.

First, consider developing a stepped-iris extraction technique that examines an expanded region junction between the iris and the material. See if evanescent higher-order modes $TE_{1,2(n-1)}$ are strongly excited to independently find a reflection coefficient.

Secondly, comparison between past techniques such as the two-thickness, two layer and two iris for sensitivity analysis can inspected. Additionally, wider source of error in Monte Carlo analysis can be extended perhaps by including other effects such as random noise. Even though, in this research sample thickness was chosen to fit the entire sample holder. This can be added if smaller samples are investigated.

Lastly, an asymmetrical stepped-iris could be manufactured where the height is reduced on only one side of the material. Additionally, extending this concept multiple shims can be devised to search for additional unique measurement.

Bibliography

1. E. J. Rothwell, "Progress In Electromagnetics Research B, Vol. 26, 121, 2010," vol. 26, no. August, pp. 1–21, 2010.

2. M. A. Kempin, "Design and analysis of an open-ended waveguide probe for material characterization," 2013. [Online]. Available: https://mospace.umsystem.edu/xmlui/handle/10355/41182

3. G. D. Dester, E. J. Rothwell, and M. J. Havrilla, "An extrapolation method for improving waveguide probe material characterization accuracy," *IEEE Microwave and Wireless Components Letters*, vol. 20, no. 5, pp. 298–300, 2010.

4. J. W. Stewart and M. J. Havrilla, "Electromagnetic Characterization of a Magnetic Material Using an Open-ended Waveguide Probe and a Rigorous Full-wave Multimode Model," *Journal of Electromagnetic Waves and Applications*, vol. 20, no. 14, pp. 2037–2052, 1 2006. [Online]. Available: http://www.tandfonline.com/doi/abs/10.1163/156939306779322693

5. G. D. Dester and E. J. Rothwell, "Two-Layer Method Theory," pp. 8–11, 2008.

6. R. E. Collin and IEEE Antennas and Propagation Society., *Field theory of guided waves*. IEEE Press, 1991.

7. C. A. Balanis, *Advanced engineering electromagnetics*. John Wiley & Sons, 2012.

8. R. E. Collin, *Foundations for microwave engineering*. IEEE Press, 2001.

9. R. F. Harrington, *Time-harmonic electromagnetic fields*. IEEE Press, 2001.

10. A. V. Kildishev and V. M. Shalaev, "Engineering Space for Light via Transformation Optics," 11 2007. [Online]. Available: http://arxiv.org/abs/0711.0183http://dx.doi.org/10.1364/OL.33.000043

11. P. Saville, "Review of Radar Absorbing Materials Defence R & D Canada Atlantic," *Defence Research and Development Canada*, no. January, p. 62, 2005.

12. Agilent, *Agilent 8510C Network Analyzer System*, 2001, no. May.

13. A. M. Nicolson and G. F. Ross, "Measurement of the Intrinsic Properties of Materials by Time-Domain Techniques," *IEEE Transactions on Instrumentation and Measurement*, vol. 19, no. 4, pp. 377–382, 11 1970. [Online]. Available: http://ieeexplore.ieee.org/document/4313932/

14. W. B. Weir, "Automatic Measurement of Complex Dielectric Constant and Permeability," *Proceedings of the IEEE*, vol. 62, no. 1, pp. 33–36, 1974.

15. A. Bogle, M. Havrilla, D. Nyquis, L. Kempel, and E. Rothwell, "Electromagnetic material characterization using a partially-filled rectangular waveguide," *Journal of Electromagnetic Waves and Applications*, vol. 19, no. 10, pp. 1291–1306, 2005.

16. J. L. Frasch and E. J. Rothwell, "A stepped waveguide technique for the characterization of conductor-backed absorbing materials," *2015 USNC-URSI Radio Science Meeting (Joint with AP-S Symposium), USNC-URSI 2015 - Proceedings*, no. 1, p. 4, 2015.

17. S. P. Dorey, "Stepped Waveguide Electromagnetic Material Characterization Technique - Storming Media." [Online]. Available: http://www.stormingmedia.us/62/6256/A625624.html

18. J. Baker-Jarvis, D. Michael, J. H. Jr, and G. Richard, "NIST Technical Note 1355-R Transmission/Reflection and Short-Circuit line Methods for Measuring Permittivity and Permeability," 1993.

Appendix A. Modal Analysis Details

1.1 Measurement Reflection 2 math details

$$\left.\begin{aligned}
\mathbf{E}_t^A &= A_{1,0}^{+,TE}\mathbf{e}_{t1,0}^{A,TE}e^{-\gamma_{z1,0}^A z} + \sum_{n=1}^{N} A_{1,2(n-1)}^{-,TE}\mathbf{e}_{t1,2(n-1)}^{A,TE}e^{\gamma_{z1,2(n-1)}^A z} \\
&\quad + \sum_{n=2}^{N} A_{1,2(n-1)}^{-,TM}\mathbf{e}_{t1,2(n-1)}^{A,TM}e^{\gamma_{z1,2(n-1)}^A z} \\
\mathbf{H}_t^A &= A_{1,0}^{+,TE}\mathbf{h}_{t1,0}^{A,TE}e^{-\gamma_{z1,0}^A z} - \sum_{n=1}^{N} A_{1,2(n-1)}^{-,TE}\mathbf{h}_{t1,2(n-1)}^{A,TE}e^{\gamma_{z1,2(n-1)}^A z} \\
&\quad - \sum_{n=2}^{N} A_{1,2(n-1)}^{-,TM}\mathbf{h}_{t1,2(n-1)}^{A,TM}e^{\gamma_{z1,2(n-1)}^A z}
\end{aligned}\right\} \quad \text{z<0} \qquad (67)$$

$$\left.\begin{aligned}
\mathbf{E}_t^B &= \sum_{n=1}^{N} B_{1,2(n-1)}^{+,TE}\mathbf{e}_{t1,2(n-1)}^{B,TE}e^{-\gamma_{z1,2(n-1)}^B z} + \sum_{n=1}^{N} B_{1,2(n-1)}^{-,TE}\mathbf{e}_{t1,2(n-1)}^{B,TE}e^{\gamma_{z1,2(n-1)}^B z} \\
&\quad + \sum_{n=2}^{N} B_{1,2(n-1)}^{+,TM}\mathbf{e}_{t1,2(n-1)}^{B,TM}e^{-\gamma_{z1,2(n-1)}^B z} + \sum_{n=2}^{N} B_{1,2(n-1)}^{-,TM}\mathbf{e}_{t1,2(n-1)}^{B,TM}e^{\gamma_{z1,2(n-1)}^B z} \\
\mathbf{H}_t^B &= \sum_{n=1}^{N} B_{1,2(n-1)}^{+,TE}\mathbf{h}_{t1,2(n-1)}^{B,TE}e^{-\gamma_{z1,2(n-1)}^B z} - \sum_{n=1}^{N} B_{1,2(n-1)}^{-,TE}\mathbf{h}_{t1,2(n-1)}^{B,TE}e^{\gamma_{z1,2(n-1)}^B z} \\
&\quad + \sum_{n=2}^{N} B_{1,2(n-1)}^{+,TM}\mathbf{h}_{t1,2(n-1)}^{B,TM}e^{-\gamma_{z1,2(n-1)}^B z} - \sum_{n=2}^{N} B_{1,2(n-1)}^{-,TM}\mathbf{h}_{t1,2(n-1)}^{B,TM}e^{\gamma_{z1,2(n-1)}^B z}
\end{aligned}\right\} \quad 0<\text{z}<\ell \qquad (68)$$

$$\left.\begin{aligned}
\mathbf{E}_t^C &= \sum_{n=1}^{N} C_{1,2(n-1)}^{+,TE}\mathbf{e}_{t1,2(n-1)}^{C,TE}e^{-\gamma_{z1,2(n-1)}^C (z-\ell)} + \sum_{n=1}^{N} C_{1,2(n-1)}^{-,TE}\mathbf{e}_{t1,2(n-1)}^{C,TE}e^{\gamma_{z1,2(n-1)}^C (z-\ell)} \\
&\quad + \sum_{n=2}^{N} C_{1,2(n-1)}^{+,TM}\mathbf{e}_{t1,2(n-1)}^{C,TM}e^{-\gamma_{z1,2(n-1)}^C (z-\ell)} + \sum_{n=2}^{N} C_{1,2(n-1)}^{-,TM}\mathbf{e}_{t1,2(n-1)}^{C,TM}e^{\gamma_{z1,2(n-1)}^C (z-\ell)} \\
\mathbf{H}_t^C &= \sum_{n=1}^{N} C_{1,2(n-1)}^{+,TE}\mathbf{h}_{t1,2(n-1)}^{C,TE}e^{-\gamma_{z1,2(n-1)}^C (z-\ell)} - \sum_{n=1}^{N} C_{1,2(n-1)}^{-,TE}\mathbf{h}_{t1,2(n-1)}^{C,TE}e^{\gamma_{z1,2(n-1)}^B (z-\ell)} \\
&\quad + \sum_{n=2}^{N} C_{1,2(n-1)}^{+,TM}\mathbf{h}_{t1,2(n-1)}^{C,TM}e^{-\gamma_{z1,2(n-1)}^C (z-\ell)} - \sum_{n=2}^{N} C_{1,2(n-1)}^{-,TM}\mathbf{h}_{t1,2(n-1)}^{C,TM}e^{\gamma_{z1,2(n-1)}^B (z-\ell)}
\end{aligned}\right\} \quad \begin{matrix}\text{z }>\ell \\ \text{z}<\ell+d\end{matrix} \qquad (69)$$

$$\mathbf{e}^{A,TE}_{1,2(n-1)} = \hat{x}(-1)^n k^A_{y2(n-1)} \sin k_{x1}x \sin k^A_{y2(n-1)}y + \hat{y}(-1)^n k_{x1} \cos k_{x1}x \cos k^A_{y2(n-1)}y$$
$$\mathbf{e}^{A,TM}_{1,2(n-1)} = \hat{x}(-1)^n k_{x1} \sin k_{x1}x \sin k^A_{y2(n-1)}y - \hat{y}(-1)^n k^A_{y2(n-1)} \cos k_{x1}x \cos k^A_{y2(n-1)}y$$
$$\mathbf{h}^{A,TE}_{t1,2(n-1)} = \frac{\hat{z} \times \mathbf{e}^{A,TE}_{t1,2(n-1)}}{Z^{A,TE}_{1,2(n-1)}},\ \mathbf{h}^{A,TM}_{t1,2(n-1)} = \frac{\hat{z} \times \mathbf{e}^{A,TM}_{t1,2(n-1)}}{Z^{A,TM}_{1,2(n-1)}} \tag{70}$$
$$Z^{A,TE}_{1,2(n-1)} = \frac{j\omega\mu_0}{\gamma^A_{z1,2(n-1)}},\ Z^{A,TM}_{1,2(n-1)} = \frac{\gamma^A_{z1,2(n-1)}}{\omega\varepsilon_0}$$
$$k_{x1} = \frac{\pi}{a},\ k^A_{y2(n-1)} = \frac{2(n-1)\pi}{b},\ \gamma^A_{z1,2(n-1)} = \sqrt{k^2_{x1} + k^{A2}_{y2(n-1)} - k^2_0}$$

$$\mathbf{e}^{B,TE}_{1,2(n-1)} = \hat{x}(-1)^n k^B_{y2(n-1)} \sin k_{x1}x \sin k^B_{y2(n-1)}y + \hat{y}(-1)^n k_{x1} \cos k_{x1}x \cos k^B_{y2(n-1)}y$$
$$\mathbf{e}^{B,TM}_{1,2(n-1)} = \hat{x}(-1)^n k_{x1} \sin k_{x1}x \sin k^B_{y2(n-1)}y - \hat{y}(-1)^n k^B_{y2(n-1)} \cos k_{x1}x \cos k^B_{y2(n-1)}y$$
$$\mathbf{h}^{B,TE}_{t1,2(n-1)} = \frac{\hat{z} \times \mathbf{e}^{B,TE}_{t1,2(n-1)}}{Z^{B,TE}_{1,2(n-1)}},\ \mathbf{h}^{B,TM}_{t1,2(n-1)} = \frac{\hat{z} \times \mathbf{e}^{B,TM}_{t1,2(n-1)}}{Z^{B,TM}_{1,2(n-1)}} \tag{71}$$
$$Z^{B,TE}_{1,2(n-1)} = \frac{j\omega\mu_B}{\gamma^B_{z1,2(n-1)}},\ Z^{B,TM}_{1,2(n-1)} = \frac{\gamma^B_{z1,2(n-1)}}{\omega\varepsilon_B}$$
$$k_{x1} = \frac{\pi}{a},\ k^B_{y2(n-1)} = \frac{2(n-1)\pi}{b},\ \gamma^B_{z1,2(n-1)} = \sqrt{k^2_{x1} + k^{B2}_{y2(n-1)} - k^2_B}$$

$$\mathbf{e}^{C,TE}_{1,2(n-1)} = \hat{x}(-1)^n k^C_{y2(n-1)} \sin k_{x1}x \sin k^C_{y2(n-1)}y + \hat{y}(-1)^n k_{x1} \cos k_{x1}x \cos k^C_{y2(n-1)}y$$
$$\mathbf{e}^{C,TM}_{1,2(n-1)} = \hat{x}(-1)^n k_{x1} \sin k_{x1}x \sin k^C_{y2(n-1)}y - \hat{y}(-1)^n k^A_{y2(n-1)} \cos k_{x1}x \cos k^C_{y2(n-1)}y$$
$$\mathbf{h}^{C,TE}_{t1,2(n-1)} = \frac{\hat{z} \times \mathbf{e}^{C,TE}_{t1,2(n-1)}}{Z^{C,TE}_{1,2(n-1)}},\ \mathbf{h}^{C,TM}_{t1,2(n-1)} = \frac{\hat{z} \times \mathbf{e}^{C,TM}_{t1,2(n-1)}}{Z^{C,TM}_{1,2(n-1)}} \tag{72}$$
$$Z^{C,TE}_{1,2(n-1)} = \frac{j\omega\mu_0\mu_r}{\gamma^C_{z1,2(n-1)}},\ Z^{C,TM}_{1,2(n-1)} = \frac{\gamma^C_{z1,2(n-1)}}{\omega\varepsilon_0\varepsilon_r}$$
$$k_{x1} = \frac{\pi}{a},\ k^C_{y2(n-1)} = \frac{2(n-1)\pi}{b},\ \gamma^C_{z1,2(n-1)} = \sqrt{k^2_{x1} + k^{C2}_{y2(n-1)} - k^2}$$

Boundary Condition # 5 (note, all BC's that follow are assumed valid in the region 0<x>a)

$$\mathbf{E}_t^C(z=\ell+d)=0\ldots 0<y<b\Rightarrow$$

$$\sum_{n=1}^{N}C_{1,2(n-1)}^{+,TE}\mathbf{e}_{t1,2(n-1)}^{C,TE}\overbrace{e^{-\gamma_{z1,2(n-1)}^{C}d}}^{P_{1,2(n-1)}^{C}}+\sum_{n=1}^{N}C_{1,2(n-1)}^{-,TE}\mathbf{e}_{t1,2(n-1)}^{C,TE}\overbrace{e^{\gamma_{z1,2(n-1)}^{C}d}}^{P_{1,2(n-1)}^{-1C}}$$

$$+\sum_{n=2}^{N}C_{1,2(n-1)}^{+,TM}\mathbf{e}_{t1,2(n-1)}^{C,TM}\overbrace{e^{-\gamma_{z1,2(n-1)}^{C}d}}^{P_{1,2(n-1)}^{C}}+\sum_{n=2}^{N}C_{1,2(n-1)}^{-,TM}\mathbf{e}_{t1,2(n-1)}^{C,TM}\overbrace{e^{\gamma_{z1,2(n-1)}^{C}d}}^{P_{1,2(n-1)}^{-1C}}=0 \tag{73}$$

Applying the testing operator $\int\limits_{-\frac{b}{2}}^{\frac{b}{2}}\int\limits_{\frac{a}{2}}^{\frac{a}{2}}\mathbf{e}_{tTE1(m-1)}^{C}\cdot\{\}\,dxdy$ to (40) leads to the result

$$\sum_{n=1}^{N}C_{1,2(n-1)}^{+,TE}P_{1,2(n-1)}^{C}\int\limits_{-\frac{b}{2}}^{\frac{b}{2}}\int\limits_{\frac{a}{2}}^{\frac{a}{2}}\mathbf{e}_{t1,2(m-1)}^{C,TE}\cdot\mathbf{e}_{t1,2(n-1)}^{C,TE}dxdy$$

$$+\sum_{n=1}^{N}C_{1,2(n-1)}^{-,TE}P_{1,2(n-1)}^{-1C}\int\limits_{-\frac{b}{2}}^{\frac{b}{2}}\int\limits_{\frac{a}{2}}^{\frac{a}{2}}\mathbf{e}_{t1,2(m-1)}^{C,TE}\cdot\mathbf{e}_{t1,2(n-1)}^{C,TE}dxdy$$

$$+\sum_{n=2}^{N}C_{1,2(n-1)}^{+,TM}P_{1,2(n-1)}^{C}\int\limits_{-\frac{b}{2}}^{\frac{b}{2}}\int\limits_{\frac{a}{2}}^{\frac{a}{2}}\mathbf{e}_{t1,2(m-1)}^{C,TE}\cdot\mathbf{e}_{1,2(n-1)}^{C,TM}dxdy$$

$$+\sum_{n=2}^{N}C_{1,2(n-1)}^{-,TM}P_{1,2(n-1)}^{-1C}\int\limits_{-\frac{b}{2}}^{\frac{b}{2}}\int\limits_{\frac{a}{2}}^{\frac{a}{2}}\mathbf{e}_{t1,2(m-1)}^{C,TE}\cdot\mathbf{e}_{t1,2(n-1)}^{C,TM}dxdy=0 \tag{74}$$

$$\int_{-\frac{b}{2}}^{\frac{b}{2}}\int_{-\frac{a}{2}}^{\frac{a}{2}} \mathbf{e}^{C,TE}_{t1,2(m-1)} \cdot \mathbf{e}^{C,TE}_{t1,2(n-1)} dxdy$$

$$= (-1)^{m+n} k^C_{y2(m-1)} k^C_{y2(n-1)} \overbrace{\int_{-\frac{a}{2}}^{\frac{a}{2}} \sin^2 k_{x1} x dx}^{\frac{a}{2}} \overbrace{\int_{-\frac{b}{2}}^{\frac{b}{2}} \sin k^c_{y2(m-1)} y \sin k^C_{y2(n-1)} y dy}^{\delta_{mn}\frac{b}{2}} \tag{75}$$

$$+ (-1)^{m+n} k^2_{x1} \overbrace{\int_{-\frac{a}{2}}^{\frac{a}{2}} \cos^2 k_{x1} x dx}^{\frac{a}{2}} \overbrace{\int_{-\frac{b}{2}}^{\frac{b}{2}} \cos k^C_{y2(m-1)} y \cos k^C_{y2(n-1)} y dy}^{\delta_{mn}\frac{b}{2}}$$

$$= \begin{cases} 0 \ldots m \neq n \\ \frac{ab}{4}(k^2_{x1} + k^{C2}_{y2(n-1)}) \ldots m = n \end{cases}$$

$$\int_{-\frac{b}{2}}^{\frac{b}{2}}\int_{-\frac{a}{2}}^{\frac{a}{2}} \mathbf{e}^{C,TE}_{t1,2(m-1)} \cdot \mathbf{e}^{C,TE}_{t1,2(n-1)} dxdy$$

$$= (-1)^{m+n} k^2_{x1} k^C_{y2(m-1)} \overbrace{\int_{-\frac{a}{2}}^{\frac{a}{2}} \sin^2 k_{x1} x dx}^{\frac{a}{2}} \overbrace{\int_{-\frac{b}{2}}^{\frac{b}{2}} \sin k^c_{y2(m-1)} y \sin k^C_{y2(n-1)} y dy}^{\delta_{mn}\frac{b}{2}} \tag{76}$$

$$- (-1)^{m+n} k_{x1} k^C_{y2(n-1)} \overbrace{\int_{-\frac{a}{2}}^{\frac{a}{2}} \cos^2 k_{x1} x dx}^{\frac{a}{2}} \overbrace{\int_{-\frac{b}{2}}^{\frac{b}{2}} \cos k^C_{y2(m-1)} y \cos k^C_{y2(n-1)} y dy}^{\delta_{m-1,n}\frac{b}{2}} = 0 \tag{77}$$

$$\Rightarrow \frac{ab}{4}(k_{x1}^2 + k_{1,2(n-1)}^{C2}\left[C_{1,2(n-1)}^{+,TE}P_{1,2(n-1)}^{C} + C_{1,2(n-1)}^{-,TE}P_{1,2(n-1)}^{-1C}\right] = 0$$
$$\Rightarrow C_{1,2(n-1)}^{-,TE} = -C_{1,2(n-1)}^{+,TE}P_{1,2(n-1)}^{C2} \ldots n = 1, \ldots, N \tag{78}$$

Applying the testing operator $\int\limits_{-\frac{b}{2}}^{\frac{b}{2}}\int\limits_{\frac{a}{2}}^{\frac{a}{2}}\mathbf{e}_{t1,2(m-1)}^{C,TM}\cdot\{\}\,dxdy$ to (40) and using an analogous set of steps leads to the anticipated result

$$\Rightarrow C_{1,2(n-1)}^{-,TM} = -C_{1,2(n-1)}^{+,TM}P_{1,2(n-1)}^{C2} \ldots n = 2, \ldots, N \tag{79}$$

$$\begin{aligned}&\sum_{n=1}^{N} M_{mn}T_{TE1(n-1)}^{C} + \sum_{n=1}^{N} N_{mn}T_{TM1(n-1)}^{C} \\ &- \sum_{n=1}^{N} O_{mn}T_{TE1(n-1)}^{B} - \sum_{n=1}^{N} P_{mn}R_{TE1(n-1)}^{B} = 0 \ldots m = 1, \ldots, N\end{aligned} \tag{80}$$

$$\int\limits_{-\frac{a}{2}}^{\frac{a}{2}} \cos^2 k_{x1}x dx = 2\int\limits_{0}^{\frac{a}{2}} \cos^2 k_{x1}x dx = 2\left(\frac{x}{2} + \frac{\sin 2k_{x1}x}{4k_{x1}}\Big|_{0}^{\frac{a}{2}}\right) = 2(\frac{a}{2} + \frac{\overbrace{\sin 2\overbrace{k_{x1}a}^{\pi}}^{0}}{4k_{x1}}) = \frac{a}{2}$$

$$\int\limits_{-\frac{a}{2}}^{\frac{a}{2}} \sin^2 k_{x1}x dx = 2\int\limits_{0}^{\frac{a}{2}} \sin^2 k_{x1}x dx = 2\left(\frac{x}{2} + \frac{\sin 2k_{x1}x}{4k_{x1}}\Big|_{0}^{\frac{a}{2}}\right) = 2(\frac{a}{2} + \frac{\overbrace{\sin 2\overbrace{k_{x1}a}^{\pi}}^{0}}{4k_{x1}}) = \frac{a}{2} \tag{81}$$

$$\begin{aligned}\int \cos my \cos nydy &= \tfrac{\sin(m-n)y}{2(m-n)} + \tfrac{\sin(m+n)y}{2(m+n)} \ldots m^2 \neq n^2 \\ \int \sin my \sin nydy &= \tfrac{\sin(m-n)y}{2(m-n)} - \tfrac{\sin(m+n)y}{2(m+n)} \ldots m^2 \neq n^2\end{aligned} \tag{82}$$

$$A_{mn} = \int\limits_{CS_B} \mathbf{e}_{t1,2(m-1)}^{B,TE} \cdot \mathbf{e}_{t1,2(n-1)}^{A,TE} dxdy \tag{83}$$

$$\int_{CS_B} \left[\hat{x}(-1)^m k^B_{y2(m-1)} \sin k_{x1} x \sin k^B_{y2(m-1)} y + \hat{y}(-1)^m k_{x1} \cos k_{x1} x \cos k^B_{y2(m-1)} y\right] \cdot \left[\hat{x}(-1)^m k^A_{y2(n-1)} \sin k_{x1} x \sin k^A_{y2(n-1)} y + \hat{y}(-1)^n k_{x1} \cos k_{x1} x \cos k^A_{y2(m-1)} y\right] \tag{84}$$

$$= (-1)^{m+n} \overbrace{\int_{-\frac{a}{2}}^{\frac{a}{2}} \sin^2 k_{x1} x dx}^{\frac{a}{2}} \overbrace{\int_{-\frac{h}{2}}^{\frac{h}{2}} \sin k^c_{y2(m-1)} y \sin k^C_{y2(n-1)} y dy}^{I_{1mn}}$$

$$+ (-1)^{m+n} \overbrace{\int_{-\frac{a}{2}}^{\frac{a}{2}} \cos^2 k_{x1} x dx}^{\frac{a}{2}} \overbrace{\int_{-\frac{b}{2}}^{\frac{b}{2}} \cos k^C_{y2(m-1)} y \cos k^C_{y2(n-1)} y dy}^{I_{2mn}}$$

$$A_{mn} = (-1)^{m+n} \tfrac{a}{2} (I_{1mn} + I_{2mn})$$

$$I_{1mn} = k^B_{y2(m-1)} y k^A_{y2(n-1)} y \int_{-\frac{h}{2}}^{\frac{h}{2}} \sin k^B_{y2(m-1)} y \sin k^A_{y2(n-1)} y dy$$

$$= \int_{-\frac{h}{2}}^{\frac{h}{2}} \sin k^B_{y2(m-1)} y \sin k^A_{y2(n-1)} y dy$$

$$= 2 \int_{0}^{-\frac{h}{2}} \sin k^B_{y2(m-1)} y \cos k^A_{y2(n-1)} y dy \tag{85}$$

$$= \begin{cases} \frac{h}{2} \ldots if k^B_{y2(m-1)} = k^A_{y2(n-1)} \\ \frac{sin[k^B_{y2(m-1)} - k^A_{y2(n-1)}]\frac{h}{2}}{k^B_{y2(m-1)} - k^A_{y2(n-1)}} - \frac{sin[k^B_{y2(m-1)} + k^A_{y2(n-1)}]\frac{h}{2}}{k^B_{y2(m-1)} + k^A_{y2(n-1)}} \ldots if k^B_{y2(m-1)} \neq k^A_{y2(n-1)} \end{cases}$$

$$
\begin{aligned}
I_{2mn} &= k_{x1)}^2 \int_{-\frac{h}{2}}^{\frac{h}{2}} \cos k_{y2(m-1)}^B y \cos k_{y2(n-1)}^A y dy \\
&= \int_{-\frac{h}{2}}^{\frac{h}{2}} \cos k_{y2(m-1)}^B y \cos k_{y2(n-1)}^A y dy \\
&= 2 \int_{0}^{-\frac{h}{2}} \cos k_{y2(m-1)}^B y \cos k_{y2(n-1)}^A y dy
\end{aligned}
\tag{86}
$$

$$
= \begin{cases} \frac{h}{2} \ldots if k_{y2(m-1)}^B = k_{y2(n-1)}^A \\ \frac{sin[k_{y2(m-1)}^B - k_{y2(n-1)}^A]\frac{h}{2}}{k_{y2(m-1)}^B - k_{y2(n-1)}^A} - \frac{sin[k_{y2(m-1)}^B + k_{y2(n-1)}^A]\frac{h}{2}}{k_{y2(m-1)}^B + k_{y2(n-1)}^A} \ldots if k_{y2(m-1)}^B \neq k_{y2(n-1)}^A \end{cases}
$$

$$
A_{mn} = (-1)^{m+n} \frac{a}{2} (I_{1mn} + I_{2mn})
$$

$$
I_{1mn} = k_{y2(m-1)}^B k_{y2(n-1)}^A \begin{cases} \frac{h}{2} \ldots if k_{y2(m-1)}^B = k_{y2(n-1)}^A \\ \frac{sin[k_{y2(m-1)}^B - k_{y2(n-1)}^A]\frac{h}{2}}{k_{y2(m-1)}^B - k_{y2(n-1)}^A} - \frac{sin[k_{y2(m-1)}^B + k_{y2(n-1)}^A]\frac{h}{2}}{k_{y2(m-1)}^B + k_{y2(n-1)}^A} \ldots \quad if k_{y2(m-1)}^B \\ \qquad\qquad\qquad\qquad\qquad\qquad\qquad\qquad\qquad\qquad \neq k_{y2(n-1)}^A \end{cases}
$$

$$
I_{2mn} = k_{x1}^2 \begin{cases} \frac{h}{2} \ldots if k_{y2(m-1)}^B = k_{y2(n-1)}^A \\ \frac{sin[k_{y2(m-1)}^B - k_{y2(n-1)}^A]\frac{h}{2}}{k_{y2(m-1)}^B - k_{y2(n-1)}^A} - \frac{sin[k_{y2(m-1)}^B + k_{y2(n-1)}^A]\frac{h}{2}}{k_{y2(m-1)}^B + k_{y2(n-1)}^A} \ldots if k_{y2(m-1)}^B \neq k_{y2(n-1)}^A \end{cases}
$$

$$
B_{mn} = \int_{CS_B} \mathbf{e}_{t1,2(m-1)}^{B,TE} \cdot \mathbf{e}_{t1,2(n-1)}^{A,TM} dx dy
\tag{87}
$$

$$\int\limits_{CS_B} \left[\hat{x}(-1)^m k^B_{y2(m-1)} \sin k_{x1} x \sin k^B_{y2(m-1)} y + \hat{y}(-1)^m k_{x1} \cos k_{x1} x \cos k^B_{y2(m-1)} y\right] \cdot \left[\hat{x}(-1)^m k^A_{y2(n-1)} \sin k_{x1} x \sin k^A_{y2(n-1)} y - \hat{y}(-1)^n k_{x1} \cos k_{x1} x \cos k^A_{y2(m-1)} y\right] \tag{88}$$

$$= (-1)^{m+n} k^2_{x1} \overbrace{\int\limits_{-\frac{a}{2}}^{\frac{a}{2}} \sin^2 k_{x1} x dx}^{\frac{a}{2}} \overbrace{\int\limits_{-\frac{h}{2}}^{\frac{h}{2}} \sin k^c_{y2(m-1)} y \sin k^C_{y2(n-1)} y dy}^{I_{3mn}}$$

$$+ (-1)^{m+n} k^2_{x1} \overbrace{\int\limits_{-\frac{a}{2}}^{\frac{a}{2}} \cos^2 k_{x1} x dx}^{\frac{a}{2}} \overbrace{\int\limits_{-\frac{b}{2}}^{\frac{b}{2}} \cos k^C_{y2(m-1)} y \cos k^C_{y2(n-1)} y dy}^{I_{4mn}}$$

$$= (-1)^{m+n} \tfrac{a}{2} (I_{3mn} - I_{4mn}) \tag{89}$$

$$B_{mn} = (-1)^{m+n} k_{x1} \tfrac{a}{2} (I_{3mn} - I_{4mn})$$

$$I_{3mn} = k^B_{y2(m-1)} \begin{cases} \frac{h}{2} \ldots if k^B_{y2(m-1)} = k^A_{y2(n-1)} \\ \frac{sin[k^B_{y2(m-1)} - k^A_{y2(n-1)}]\frac{h}{2}}{k^B_{y2(m-1)} - k^A_{y2(n-1)}} - \frac{sin[k^B_{y2(m-1)} + k^A_{y2(n-1)}]\frac{h}{2}}{k^B_{y2(m-1)} + k^A_{y2(n-1)}} \ldots & if k^B_{y2(m-1)} \\ & \neq k^A_{y2(n-1)} \end{cases}$$

$$I_{4mn} = k^A_{y2(n-1)} \begin{cases} \frac{h}{2} \ldots if k^B_{y2(m-1)} = k^A_{y2(n-1)} \\ \frac{sin[k^B_{y2(m-1)} - k^A_{y2(n-1)}]\frac{h}{2}}{k^B_{y2(m-1)} - k^A_{y2(n-1)}} - \frac{sin[k^B_{y2(m-1)} + k^A_{y2(n-1)}]\frac{h}{2}}{k^B_{y2(m-1)} + k^A_{y2(n-1)}} \ldots & if k^B_{y2(m-1)} \\ & \neq k^A_{y2(n-1)} \end{cases}$$

$$C_{mn} = \int\limits_{CS_B} \mathbf{e}^{B,TE}_{t1,2(m-1)} \cdot \mathbf{e}^{A,TE}_{t1,2(n-1)} dxdy \tag{90}$$

$$\int\limits_{CS_B} \left[\hat{x}(-1)^m k^B_{y2(m-1)} \sin k_{x1}x \sin k^B_{y2(m-1)}y + \hat{y}(-1)^m k_{x1} \cos k_{x1}x \cos k^B_{y2(m-1)}y\right] \cdot \left[\hat{x}(-1)^m k^A_{y2(n-1)} \sin k_{x1}x \sin k^A_{y2(n-1)}y + \hat{y}(-1)^n k_{x1} \cos k_{x1}x \cos k^A_{y2(m-1)}y\right] \tag{91}$$

$$= (-1)^{m+n} k^B_{y2(m-1)} k^B_{y2(n-1)} \overbrace{\int\limits_{-\frac{a}{2}}^{\frac{a}{2}} \sin^2 k_{x1}x dx}^{\frac{a}{2}} \overbrace{\int\limits_{-\frac{h}{2}}^{\frac{h}{2}} \sin k^c_{y2(m-1)}y \sin k^C_{y2(n-1)}y dy}^{\frac{h}{2}\delta_{mn}}$$

$$+ (-1)^{m+n} k^2_{x1} \overbrace{\int\limits_{-\frac{a}{2}}^{\frac{a}{2}} \cos^2 k_{x1}x dx}^{\frac{a}{2}} \overbrace{\int\limits_{-\frac{b}{2}}^{\frac{b}{2}} \cos k^C_{y2(m-1)}y \cos k^C_{y2(n-1)}y dy}^{\frac{h}{2}\delta_{mn}}$$

$$C_{mn} = \begin{cases} \frac{ah}{4}(k^2_{x1} + k^{B2}_{y2(m-1)} \ldots if m = n \\ 0 \ldots if m \neq n \end{cases} \tag{92}$$

$$D_{mn} = \int\limits_{CS_B} \mathbf{e}^{B,TM}_{t1,2(m-1)} \cdot \mathbf{e}^{A,TE}_{t1,2(n-1)} dxdy \tag{93}$$

$$\int\limits_{CS_B} \left[\hat{x}(-1)^m k^B_{y2(m-1)} \sin k_{x1}x \sin k^B_{y2(m-1)}y - \hat{y}(-1)^m k_{x1} \cos k_{x1}x \cos k^B_{y2(m-1)}y\right] \cdot \left[\hat{x}(-1)^m k^A_{y2(n-1)} \sin k_{x1}x \sin k^A_{y2(n-1)}y + \hat{y}(-1)^n k_{x1} \cos k_{x1}x \cos k^A_{y2(m-1)}y\right] \tag{94}$$

$$= (-1)^{m+n} k_{x1}^2 \overbrace{\int_{-\frac{a}{2}}^{\frac{a}{2}} \sin^2 k_{x1} x dx}^{\frac{a}{2}} \overbrace{\int_{-\frac{h}{2}}^{\frac{h}{2}} \sin k^c_{y2(m-1)} y \sin k^C_{y2(n-1)} y dy}^{I_{5mn}}$$

$$+ (-1)^{m+n} k_{x1}^2 \overbrace{\int_{-\frac{a}{2}}^{\frac{a}{2}} \cos^2 k_{x1} x dx}^{\frac{a}{2}} \overbrace{\int_{-\frac{b}{2}}^{\frac{b}{2}} \cos k^C_{y2(m-1)} y \cos k^C_{y2(n-1)} y dy}^{I_{6mn}}$$

$$= (-1)^{m+n} \tfrac{a}{2} (I_{5mn} - I_{6mn}) \tag{95}$$

$$D_{mn} = (-1)^{m+n} k_{x1} \tfrac{a}{2} (I_{5mn} - I_{6mn})$$

$$I_{5mn} = k^A_{y2(n-1)} \begin{cases} \frac{h}{2} \dots if k^B_{y2(m-1)} = k^A_{y2(n-1)} \\ \frac{sin[k^B_{y2(m-1)} - k^A_{y2(n-1)}]\frac{h}{2}}{k^B_{y2(m-1)} - k^A_{y2(n-1)}} - \frac{sin[k^B_{y2(m-1)} + k^A_{y2(n-1)}]\frac{h}{2}}{k^B_{y2(m-1)} + k^A_{y2(n-1)}} \dots & if k^B_{y2(m-1)} \\ & \neq k^A_{y2(n-1)} \end{cases}$$

$$I_{6mn} = k^B_{y2(m-1)} \begin{cases} \frac{h}{2} \dots if k^B_{y2(m-1)} = k^A_{y2(n-1)} \\ \frac{sin[k^B_{y2(m-1)} - k^A_{y2(n-1)}]\frac{h}{2}}{k^B_{y2(m-1)} - k^A_{y2(n-1)}} - \frac{sin[k^B_{y2(m-1)} + k^A_{y2(n-1)}]\frac{h}{2}}{k^B_{y2(m-1)} + k^A_{y2(n-1)}} \dots & if k^B_{y2(m-1)} \\ & \neq k^A_{y2(n-1)} \end{cases}$$

$$E_{mn} = \int_{CS_B} \mathbf{e}^{B,TM}_{t1,2(m-1)} \cdot \mathbf{e}^{A,TM}_{t1,2(n-1)} dxdy \tag{96}$$

$$\int_{CS_B} \left[\hat{x}(-1)^m k^B_{y2(m-1)} \sin k_{x1} x \sin k^B_{y2(m-1)} y - \hat{y}(-1)^m k_{x1} \cos k_{x1} x \cos k^B_{y2(m-1)} y\right]$$
$$\cdot \left[\hat{x}(-1)^m k^A_{y2(n-1)} \sin k_{x1} x \sin k^A_{y2(n-1)} y - \hat{y}(-1)^n k_{x1} \cos k_{x1} x \cos k^A_{y2(m-1)} y\right] \tag{97}$$

$$= (-1)^{m+n} \overbrace{\int_{-\frac{a}{2}}^{\frac{a}{2}} \sin^2 k_{x1} x dx}^{\frac{a}{2}} \overbrace{\int_{-\frac{h}{2}}^{\frac{h}{2}} \sin k^c_{y2(m-1)} y \sin k^C_{y2(n-1)} y dy}^{I_{7mn}}$$

$$+ (-1)^{m+n} \overbrace{\int_{-\frac{a}{2}}^{\frac{a}{2}} \cos^2 k_{x1} x dx}^{\frac{a}{2}} \overbrace{\int_{-\frac{b}{2}}^{\frac{b}{2}} \cos k^C_{y2(m-1)} y \cos k^C_{y2(n-1)} y dy}^{I_{8mn}}$$

$$= (-1)^{m+n} \tfrac{a}{2} (I_{5mn} - I_{6mn}) \tag{98}$$

$$E_{mn} = (-1)^{m+n} k_{x1} \tfrac{a}{2} (I_{7mn} - I_{8mn})$$

$$I_{7mn} = k^2_{x1)} \begin{cases} \frac{h}{2} \dots if k^B_{y2(m-1)} = k^A_{y2(n-1)} \\ \frac{sin[k^B_{y2(m-1)} - k^A_{y2(n-1)}]\frac{h}{2}}{k^B_{y2(m-1)} - k^A_{y2(n-1)}} - \frac{sin[k^B_{y2(m-1)} + k^A_{y2(n-1)}]\frac{h}{2}}{k^B_{y2(m-1)} + k^A_{y2(n-1)}} \dots & if k^B_{y2(m-1)} \\ & \neq k^A_{y2(n-1)} \end{cases}$$

$$I_{8mn} = k^B_{y2(m-1)} k^A_{y2(n-1)} \begin{cases} \frac{h}{2} \dots if k^B_{y2(m-1)} = k^A_{y2(n-1)} \\ \frac{sin[k^B_{y2(m-1)} - k^A_{y2(n-1)}]\frac{h}{2}}{k^B_{y2(m-1)} - k^A_{y2(n-1)}} - \frac{sin[k^B_{y2(m-1)} + k^A_{y2(n-1)}]\frac{h}{2}}{k^B_{y2(m-1)} + k^A_{y2(n-1)}} \dots & if k^B_{y2(m-1)} \\ & \neq k^A_{y2(n-1)} \end{cases}$$

$$F_{mn} = \int_{CS_B} \mathbf{e}^{B,TE}_{t1,2(m-1)} \cdot \mathbf{e}^{A,TE}_{t1,2(n-1)} dxdy \tag{99}$$

$$\int_{CS_B} \left[\hat{x}(-1)^m k^B_{y2(m-1)} \sin k_{x1} x \sin k^B_{y2(m-1)} y - \hat{y}(-1)^m k_{x1} \cos k_{x1} x \cos k^B_{y2(m-1)} y\right]$$
$$\cdot \left[\hat{x}(-1)^m k^A_{y2(n-1)} \sin k_{x1} x \sin k^A_{y2(n-1)} y - \hat{y}(-1)^n k_{x1} \cos k_{x1} x \cos k^A_{y2(m-1)} y\right] \tag{100}$$

$$= (-1)^{m+n} k^B_{y2(m-1)} k^B_{y2(n-1)} \overbrace{\int_{-\frac{a}{2}}^{\frac{a}{2}} \sin^2 k_{x1} x dx}^{\frac{a}{2}} \overbrace{\int_{-\frac{h}{2}}^{\frac{h}{2}} \sin k^c_{y2(m-1)} y \sin k^C_{y2(n-1)} y dy}^{\frac{h}{2}\delta_{mn}}$$

$$+ (-1)^{m+n} k^2_{x1} \overbrace{\int_{-\frac{a}{2}}^{\frac{a}{2}} \cos^2 k_{x1} x dx}^{\frac{a}{2}} \overbrace{\int_{-\frac{b}{2}}^{\frac{b}{2}} \cos k^C_{y2(m-1)} y \cos k^C_{y2(n-1)} y dy}^{\frac{h}{2}\delta_{mn}}$$

$$F_{mn} = \begin{cases} \frac{ah}{4}(k^2_{x1} + k^{B2}_{y2(m-1)} \dots if m = n \\ 0 \dots if m \neq n \end{cases} \tag{101}$$

$$\begin{aligned} G_{mn} &= \int_{CS_B} \mathbf{h}^{B,TE}_{1,2(m-1)} \cdot \mathbf{h}^{A,TE}_{1,2(n-1)} ds \\ &= \frac{1}{Z^{B,TE}_{1,2(m-1)} Z^{A,TE}_{1,2(n-1)}} \int_{CS_B} \hat{z} \times e^{B,TE}_{1,2(m-1)} \cdot \hat{z} \times e^{A,TE}_{1,2(n-1)} ds \\ &= \frac{1}{Z^{B,TE}_{1,2(m-1)} Z^{A,TE}_{1,2(n-1)}} \overbrace{\int_{CS_B} e^{B,TE}_{1,2(m-1)} \cdot e^{A,TE}_{1,2(n-1)} ds}^{A_{mn}} \end{aligned} \tag{102}$$

$$G_{mn} = \frac{A_{mn}}{Z^{B,TE}_{1,2(m-1)} Z^{A,TE}_{1,2(n-1)}} \tag{103}$$

$$\begin{aligned} H_{mn} &= \int_{CS_B} \mathbf{h}^{B,TE}_{1,2(m-1)} \cdot \mathbf{h}^{A,TM}_{1,2(n-1)} ds \\ &= \frac{1}{Z^{B,TE}_{1,2(m-1)} Z^{A,TM}_{1,2(n-1)}} \overbrace{\int_{CS_B} e^{B,TE}_{1,2(m-1)} \cdot e^{A,TM}_{1,2(n-1)} ds}^{B_{mn}} \end{aligned}$$

$$H_{mn} = \frac{B_{mn}}{Z^{B,TE}_{1,2(m-1)} Z^{A,TE}_{1,2(n-1)}} \tag{104}$$

$$I_{mn} = \int\limits_{CS_B} \mathbf{h}^{B,TE}_{1,2(m-1)} \cdot \mathbf{h}^{B,TE}_{1,2(n-1)} ds = \frac{C_{mn}}{Z^{B,TE}_{1,2(m-1)} Z^{B,TE}_{1,2(n-1)}} \tag{105}$$

$$J_{mn} = \int\limits_{CS_B} \mathbf{h}^{B,TM}_{1,2(m-1)} \cdot \mathbf{h}^{A,TE}_{1,2(n-1)} ds = \frac{D_{mn}}{Z^{B,TM}_{1,2(m-1)} Z^{A,TE}_{1,2(n-1)}} \tag{106}$$

$$K_{mn} = \int\limits_{CS_B} \mathbf{h}^{B,TM}_{1,2(m-1)} \cdot \mathbf{h}^{A,TM}_{1,2(n-1)} ds = \frac{E_{mn}}{Z^{B,TM}_{1,2(m-1)} Z^{A,TM}_{1,2(n-1)}} \tag{107}$$

$$L_{mn} = \int\limits_{CS_B} \mathbf{h}^{B,TM}_{1,2(m-1)} \cdot \mathbf{h}^{B,TM}_{1,2(n-1)} ds = \frac{F_{mn}}{Z^{B,TM}_{1,2(m-1)} Z^{B,TM}_{1,2(n-1)}} \tag{108}$$

$$M_{mn} = [1 - P^{C2}_{1,2(n-1)}] \int\limits_{CS_B} \mathbf{e}^{B,TE}_{1,2(m-1)} \cdot \overbrace{\mathbf{e}^{C,TE}_{1,2(n-1)} ds}^{e^{A,TE}_{1,2(n-1)}} = [1 - P^{C2}_{1,2(n-1)}] A_{mn} \tag{109}$$

$$N_{mn} = [1 - P^{C2}_{1,2(n-1)}] \int\limits_{CS_B} \mathbf{e}^{B,TE}_{1,2(m-1)} \cdot \mathbf{e}^{C,TM}_{1,2(n-1)} ds = [1 - P^{C2}_{1,2(n-1)}] B_{mn} \tag{110}$$

$$O_{mn} = P^{B}_{1,2(n-1)} \int\limits_{CS_B} \mathbf{e}^{B,TE}_{1,2(m-1)} \cdot \mathbf{e}^{B,TE}_{1,2(n-1)} ds = P^{B}_{1,2(n-1)} C_{mn} \tag{111}$$

$$P_{mn} = P^{-1B}_{1,2(n-1)} \int\limits_{CS_B} \mathbf{e}^{B,TE}_{1,2(m-1)} \cdot \mathbf{e}^{B,TE}_{1,2(n-1)} ds = P^{-1B}_{1,2(n-1)} C_{mn} \tag{112}$$

$$Q_{mn} = [1 - P^{C2}_{1,2(n-1)}] \int\limits_{CS_B} \mathbf{e}^{B,TM}_{1,2(m-1)} \cdot \mathbf{e}^{C,TE}_{1,2(n-1)} ds = [1 - P^{C2}_{1,2(n-1)}] D_{mn} \tag{113}$$

$$R_{mn} = [1 - P^{C2}_{1,2(n-1)}] \int\limits_{CS_B} \mathbf{e}^{B,TM}_{1,2(m-1)} \cdot \mathbf{e}^{C,TM}_{1,2(n-1)} ds = [1 - P^{C2}_{1,2(n-1)}] E_{mn} \tag{114}$$

$$S_{mn} = P^{B}_{1,2(n-1)} \int\limits_{CS_B} \mathbf{e}^{B,TM}_{1,2(m-1)} \cdot \mathbf{e}^{B,TM}_{1,2(n-1)} ds = P^{B}_{1,2(n-1)} F_{mn} \tag{115}$$

$$T_{mn} = P^{-1B}_{1,2(n-1)} \int\limits_{CS_B} \mathbf{e}^{B,TM}_{1,2(m-1)} \cdot \mathbf{e}^{B,TM}_{1,2(n-1)} ds = P^{-1B}_{1,2(n-1)} F_{mn} \tag{116}$$

$$U_{mn} = [1 + P^{C2}_{1,2(n-1)}] \int\limits_{CS_B} \mathbf{h}^{B,TE}_{1,2(m-1)} \cdot \mathbf{h}^{C,TE}_{1,2(n-1)} ds = \frac{[1+P^{C2}_{1,2(n-1)}]A_{mn}}{Z^{B,TE}_{1,2(m-1)} Z^{C,TE}_{1,2(m-1)}} \tag{117}$$

$$V_{mn} = [1 + P^{C2}_{1,2(n-1)}] \int\limits_{CS_B} \mathbf{h}^{B,TE}_{1,2(m-1)} \cdot \mathbf{h}^{C,TM}_{1,2(n-1)} ds = \frac{[1+P^{C2}_{1,2(n-1)}]B_{mn}}{Z^{B,TE}_{1,2(m-1)} Z^{C,TM}_{1,2(m-1)}} \tag{118}$$

$$W_{mn} = P^{B}_{1,2(n-1)} \int\limits_{CS_B} \mathbf{h}^{B,TE}_{1,2(m-1)} \cdot \mathbf{h}^{B,TE}_{1,2(n-1)} ds = \frac{P^{B}_{1,2(n-1)}]C_{mn}}{Z^{B,TE}_{1,2(m-1)} Z^{B,TE}_{1,2(m-1)}} \tag{119}$$

$$X_{mn} = P^{-1B}_{1,2(n-1)} \int\limits_{CS_B} \mathbf{h}^{B,TE}_{1,2(m-1)} \cdot \mathbf{h}^{B,TE}_{1,2(n-1)} ds = \frac{P^{-1B}_{1,2(n-1)}]C_{mn}}{Z^{B,TE}_{1,2(m-1)} Z^{B,TE}_{1,2(m-1)}} \tag{120}$$

$$Y_{mn} = [1 + P^{C2}_{1,2(n-1)}] \int\limits_{CS_B} \mathbf{h}^{B,TM}_{1,2(m-1)} \cdot \mathbf{h}^{C,TE}_{1,2(n-1)} ds = \frac{[1+P^{C2}_{1,2(n-1)}]D_{mn}}{Z^{B,TM}_{1,2(m-1)} Z^{C,TE}_{1,2(m-1)}} \tag{121}$$

$$Z_{mn} = [1 + P^{C2}_{1,2(n-1)}] \int\limits_{CS_B} \mathbf{h}^{B,TM}_{1,2(m-1)} \cdot \mathbf{h}^{C,TM}_{1,2(n-1)} ds = \frac{[1+P^{C2}_{1,2(n-1)}]E_{mn}}{Z^{B,TM}_{1,2(m-1)} Z^{C,TM}_{1,2(m-1)}} \tag{122}$$

$$\Gamma_{mn} = P^{B}_{1,2(n-1)} \int\limits_{CS_B} \mathbf{h}^{B,TM}_{1,2(m-1)} \cdot \mathbf{h}^{B,TM}_{1,2(n-1)} ds = \frac{P^{B}_{1,2(n-1)}]F_{mn}}{Z^{B,TM}_{1,2(m-1)} Z^{B,TM}_{1,2(m-1)}} \tag{123}$$

$$\Delta_{mn} = P^{-1B}_{1,2(n-1)} \int\limits_{CS_B} \mathbf{h}^{B,TM}_{1,2(m-1)} \cdot \mathbf{h}^{B,TM}_{1,2(n-1)} ds = \frac{P^{-1B}_{1,2(n-1)}]F_{mn}}{Z^{B,TM}_{1,2(m-1)} Z^{B,TM}_{1,2(m-1)}} \tag{124}$$

What if $h = b$ and $\ell = 0$

$$\begin{bmatrix} A_{11} & -C_{11} & -C_{11} & 0 \\ G_{11} & I_{mn} & -I_{mn} & 0 \\ 0 & -O_{mn} & -P_{mn} & M_{mn} \\ 0 & -W_{mn} & X_{mn} & U_{mn} \end{bmatrix} \begin{bmatrix} R_{10}^{A,TE} \\ T_{10}^{B,TE} \\ R_{10}^{B,TE} \\ T_{10}^{C,TE} \end{bmatrix} = \begin{bmatrix} -A_{11} \\ G_{11} \\ 0 \\ 0 \end{bmatrix} \Rightarrow R_{10}^{A,TE} = \frac{R-P^2}{1-RP^2} = S_{11}^{(1)} \ldots asexpected \tag{125}$$

REPORT DOCUMENTATION PAGE

Form Approved
OMB No. 0704–0188

1. REPORT DATE *(DD–MM–YYYY)*	2. REPORT TYPE	3. DATES COVERED *(From — To)*
03–21–2019	Master's Thesis	Sept 2017 — Mar 2019

4. TITLE AND SUBTITLE

Electromagnetic characterization of conductor-backed media using stepped rectangular waveguide

5a. CONTRACT NUMBER

5b. GRANT NUMBER

5c. PROGRAM ELEMENT NUMBER

6. AUTHOR(S)

Captain Avian Y. Hughes

5d. PROJECT NUMBER

5e. TASK NUMBER

5f. WORK UNIT NUMBER

7. PERFORMING ORGANIZATION NAME(S) AND ADDRESS(ES)

Air Force Institute of Technology
Graduate School of Engineering and Management (AFIT/EN)
2950 Hobson Way
WPAFB OH 45433-7765

8. PERFORMING ORGANIZATION REPORT NUMBER

AFIT-ENG-MS-19-M-033

9. SPONSORING / MONITORING AGENCY NAME(S) AND ADDRESS(ES)

Air Force Research Laboratory
2950 Hobson Way
WPAFB OH 45433-7765
DSN 271-0690, COMM 937-255-3636
Email: avian.hughes@afit.edu

10. SPONSOR/MONITOR'S ACRONYM(S)

AFRL/RYS

11. SPONSOR/MONITOR'S REPORT NUMBER(S)

12. DISTRIBUTION / AVAILABILITY STATEMENT

DISTRIBUTION STATEMENT A:
APPROVED FOR PUBLIC RELEASE; DISTRIBUTION UNLIMITED.

13. SUPPLEMENTARY NOTES

14. ABSTRACT

A new single stepped-iris waveguide technique is used to nondestructively determine the permittivity and permeability of conductor-backed media.This thesis will demonstrate a proof-of-concept that obtains two independent reflection measurements with a magnetic radar absorbing material. Using a two measurement procedure, in which, the first measurement, will apply a single rectangular waveguide to a known conductor-backed material under test and the second measurement, will insert a stepped-iris reducing the aperture to retrieve two independent electromagnetic properties. The theoretical reflection coefficients are obtained using a full-wave solution combined with a mode matching method at all regions. Additionally, a root search algorithm is used to extract electromagnetic properties by comparing the theoretical and experimentally measured reflection coefficients. The experimental measurements of a commercial magram using a network analyzer will demonstrate the feasibility of the stepped-iris approach. Plots of the extracted permittivity and permeability of the MUT are analyzed to validate the stepped-iris material characterization technique.

15. SUBJECT TERMS

Electromagnetic properties, permittivity, permeability, magnetic radar absorbing material, Vector Network Analyzer, rectangular waveguide, single stepped-iris technique, conductor-backed media

16. SECURITY CLASSIFICATION OF:			17. LIMITATION OF ABSTRACT	18. NUMBER OF PAGES	19a. NAME OF RESPONSIBLE PERSON
a. REPORT	b. ABSTRACT	c. THIS PAGE			Dr. M. J. Havrilla, AFIT/ENG
UU	UU	UU	UU	91	19b. TELEPHONE NUMBER *(include area code)* (937) 255-3636, x4555; avian.huges@afit.edu